

# *Two-way feedback between the Madden–Julian Oscillation and diurnal warm layers in a coupled ocean–atmosphere model*

Article

Published Version

Creative Commons: Attribution 4.0 (CC-BY)

Open Access

Karlowska, E. ORCID: <https://orcid.org/0000-0003-2401-0871>, Matthews, A. J., Webber, B. G. M., Graham, T. and Xavier, P. (2024) Two-way feedback between the Madden–Julian Oscillation and diurnal warm layers in a coupled ocean–atmosphere model. Quarterly Journal of the Royal Meteorological Society, 150 (764). pp. 4113-4132. ISSN 1477-870X doi: 10.1002/qj.4807 Available at <https://centaur.reading.ac.uk/119898/>

It is advisable to refer to the publisher's version if you intend to cite from the work. See [Guidance on citing](#).

To link to this article DOI: <http://dx.doi.org/10.1002/qj.4807>

Publisher: Royal Meteorological Society

All outputs in CentAUR are protected by Intellectual Property Rights law, including copyright law. Copyright and IPR is retained by the creators or other copyright holders. Terms and conditions for use of this material are defined in the [End User Agreement](#).

[www.reading.ac.uk/centaur](http://www.reading.ac.uk/centaur)

## **CentAUR**

Central Archive at the University of Reading

Reading's research outputs online

## RESEARCH ARTICLE

# Two-way feedback between the Madden–Julian Oscillation and diurnal warm layers in a coupled ocean–atmosphere model

Eliza Karłowska<sup>1,2</sup>  | Adrian J. Matthews<sup>3</sup>  | Benjamin G. M. Webber<sup>1</sup>  |  
Tim Graham<sup>2</sup> | Prince Xavier<sup>2</sup>

<sup>1</sup>Centre for Ocean and Atmospheric Sciences, School of Environmental Sciences, University of East Anglia, Norwich, UK

<sup>2</sup>Hadley Centre, Met Office, Exeter, UK

<sup>3</sup>Centre for Ocean and Atmospheric Sciences, School of Environmental Sciences and School of Mathematics, University of East Anglia, Norwich, UK

## Correspondence

Eliza Karłowska, School of Environmental Sciences, University of East Anglia, Norwich, UK.

Email: [e.karlowska@uea.ac.uk](mailto:e.karlowska@uea.ac.uk)

## Funding information

ARIES DTP, Grant/Award Number: NE/S007334/1; TerraMaris project, Grant/Award Number: NE/R016704/1

## Abstract

Diurnal warm layers develop in the upper ocean on sunny days with low surface wind speeds. They rectify intraseasonal sea-surface temperatures (SSTs), potentially impacting intraseasonal weather patterns such as the Madden–Julian Oscillation (MJO). Here we analyse 15-lead-day forecast composites of coupled ocean–atmosphere and atmosphere-only numerical weather prediction (NWP) models of the UK Met Office to reveal that the presence of diurnal warming of SST (dSST) leads to a faster MJO propagation in the coupled model compared with the atmosphere-only model. To test the feedback between the MJO and the dSST, we designed a set of experiments with instantaneous vertical mixing over the top 5 or 10 m of the ocean component of the coupled model. Weaker dSST in the mixing experiments leads to a slower MJO over 15 lead days. The dSST produces a 3% increase in the MJO phase speed between the coupled and the atmosphere-only model. An additional 5% increase is found for other coupling effects, unrelated to the dSST. A two-way feedback manifests in the coupled model over the 15 lead days of the forecast between the MJO and the dSST. The MJO regime dictates the strength of the dSST and the dSST rectifies the intraseasonal anomalies of SST in the coupled model. Stronger dSST in the coupled model leads to stronger intraseasonal anomalies of SST. The MJO convection responds to these SSTs on a seven-lead-day timescale, and feeds back into the SST anomalies within the next three lead days. Overall, this study demonstrates the importance of high vertical resolution in the upper ocean for predicting the eastward propagation of the MJO in an NWP setting, which is potentially impactful for seasonal predictions and climate projections, should this feedback be unrepresented in the models.

## KEYWORDS

diurnal warm layers, Madden–Julian Oscillation, ocean–atmosphere coupling, tropical weather prediction

## 1 | INTRODUCTION

The Indo-Pacific warm-pool region is the largest region of warm sea-surface temperatures (SSTs) on Earth, spanning the equatorial Indian Ocean, the Maritime Continent (MC: Indonesia, Borneo, New Guinea) and the equatorial western Pacific. It is characterised by SSTs exceeding 28 °C (e.g., Yan *et al.*, 1992), and plays a major role in modulating the global atmospheric circulation (e.g., Kim *et al.*, 2020). The intraseasonal SST anomalies over the warm-pool region influence intraseasonal weather patterns such as the Madden–Julian Oscillation (MJO). The MJO comprises an envelope of enhanced and suppressed convection and is the major component of tropical weather variability on intraseasonal timescales (Madden & Julian, 1971, 1972). It originates in the western Indian Ocean and travels eastward at a  $\sim 5 \text{ m} \cdot \text{s}^{-1}$  phase speed, often crossing into the MC and dissipating over the Pacific.

The canonical evolution of the MJO can be described by a phase-lag relationship between the MJO convective anomalies and the intraseasonal SST anomalies over the warm-pool region (e.g., Hendon & Glick, 1997; Woolnough *et al.*, 2000). Positive SST anomalies destabilise the atmosphere via surface flux exchanges, increasing the near-surface moisture and temperature gradients and promoting moist convection. Such SST anomalies are observed approximately 1 week prior to the MJO convection over the warm-pool region. During the convectively active phase of the MJO, decreased solar radiation (due to higher cloud cover) and increased latent heat flux (due to higher surface winds) lead to cooler anomalies of SST, located to the west of the MJO. This pattern of warm SST anomalies to the east and cold SST anomalies to the west evolves along the eastward-propagating MJO, lagging the MJO by a quarter of the MJO cycle. This canonical evolution of the MJO convective signal can be reproduced in atmosphere-only models forced with MJO-like SST anomalies (Matthews, 2004; Woolnough *et al.*, 2001).

There is growing evidence that short-timescale (diurnal) variations in SSTs affect the ocean–atmosphere interactions on MJO timescales. For example, the study by Yan *et al.* (2021) of the global tropical moored buoy array revealed that the diurnal variability of SST rectifies the intraseasonal variability of SST. Itterly *et al.* (2021) showed that diurnal air–sea exchanges in the warm-pool region influence the moist static energy budget prior to the onset of MJO convection. To add to the complexity, the MJO conditions themselves alter the diurnal variability of the SST (Anderson *et al.*, 1996; Bellenger & Duvel, 2009; Itterly *et al.*, 2021; Matthews *et al.*, 2014). The top few metres of the ocean are prone to the development of diurnal warm layers on days with low cloud cover and low surface wind speeds (Matthews *et al.*, 2014). Such layers often increase

the daily mean SST by  $>1$  °C and are predicted to develop on approximately 30% of the days in the warm-pool region (Matthews *et al.*, 2014). Suppressed MJO conditions favour the development of such layers (e.g., Itterly *et al.*, 2021). Observations show that the increase in daily mean SST associated with the development of diurnal warm layers affects turbulent air–sea fluxes, leading to an increase in the moist static energy ahead of the MJO and to the formation of cumulus convection (Ruppert & Johnson, 2015).

The diurnal variability of the SST can be altered artificially in coupled ocean–atmosphere models by changing the coupling frequency (e.g., Bernie *et al.*, 2007; Hsu *et al.*, 2019; Seo *et al.*, 2014) or changing the near-surface vertical resolution of the ocean model (e.g., Ge *et al.*, 2017; Tseng *et al.*, 2015; Woolnough *et al.*, 2007). For example, Bernie *et al.* (2007) showed that an increase in the coupling frequency generates stronger variability of the SST, leading to a stronger MJO response. Following this study, Bernie *et al.* (2008) found that an increased diurnal variability of SST in a coupled climate model led to a higher daily mean SST and stronger MJO projections compared with the atmosphere-only version of this model. Increased coupling frequency can also improve the phase of the diurnal cycle of surface fluxes (Hsu *et al.*, 2019; Seo *et al.*, 2014). While a more accurate diurnal cycle of surface fluxes in the study of Seo *et al.* (2014) led to stronger SST variability and stronger MJO convection in their coupled model, Hsu *et al.* (2019) found that the near-surface resolution of their ocean model led to stronger changes in SSTs (and surface fluxes) than the effects of the coupling frequency on SSTs. High near-surface resolution of the ocean generally increases daily mean SSTs and improves the MJO predictions in models (e.g., Ge *et al.*, 2017; Tseng *et al.*, 2015; Woolnough *et al.*, 2007). In particular, higher near-surface resolution can increase SSTs ahead of the MJO, resulting in the preconditioning of deep convection through increased low-level moisture (Tseng *et al.*, 2015).

MJO prediction still remains a challenge in the modelling community (e.g., Ahn *et al.*, 2020; Vitart, 2017). Many models simulate a slower MJO than observations suggest (e.g., Kim *et al.*, 2014; Kim *et al.*, 2019; Vitart, 2017; Xiang *et al.*, 2015). However, Karłowska *et al.* (2024) showed that the global coupled ocean–atmosphere numerical weather prediction (NWP) model of the UK Met Office, in contrast to most models, predicts that the MJO propagates faster than in both observations and the atmosphere-only version of this model. An increase of 12% in the MJO phase speed was recorded in the coupled model compared with the atmosphere-only model over a seven-lead-day period. Karłowska *et al.* (2024) hypothesised that this increase in MJO phase speed was caused by a strong diurnal cycle of SST present in the coupled model, absent from the atmosphere-only model, which



utilises persisted foundation SST. In this study, we confirm their hypothesis through model sensitivity experiments. We impose instantaneous mixing in the top 5 or 10 m of the ocean model component to mute the diurnal warming of SST in the coupled model, and quantify its contribution to the MJO phase-speed increase between the coupled and atmosphere-only models. In Section 2, the model specifications, data, methodology, and experimental setup are described. In Section 3, we present the MJO performance for all model runs, describe a two-way feedback between the MJO and diurnal warm layers in the coupled model, and investigate the diurnal warming effect on the mean state of the coupled model. Discussion and conclusions follow in Section 4.

## 2 | DATA AND METHODS

### 2.1 | Model specifications

The data used in this study were generated with the coupled ocean–atmosphere and the atmosphere-only NWP systems of the UK Met Office. Both models were run in a hindcast mode for a five-year period between May 1, 2016 and May 31, 2021, yielding 1857 forecast initialisations. Each model was initialised at 0000 UTC and integrated out to 15 lead days. Both models used the same atmosphere and land components, with the addition of the ocean and sea-ice component for the coupled version. Due to computational expense, the models used in this study were of lower atmospheric horizontal resolution than the operational versions of these models running at the time at the Met Office. Some of the operational changes were applied to the models on September 25, 2018 (see Table 1 for detailed model versions and their references). The horizontal resolution of the atmosphere component was N216 (0.83° longitude and 0.56° latitude) from May 1, 2016–September 24, 2018, then N320 (0.57° longitude and 0.38° latitude) from September 25, 2018–May 31, 2021. The same cumulus parameterisation scheme, with shallow, mid-level, and deep convection (Gregory &

Allen, 1991; Gregory & Rowntree, 1990), is used across all the horizontal resolutions studied here and in Karlowska *et al.* (2024).

The atmosphere component of the coupled model is coupled to the Nucleus for European Modelling of the Ocean (NEMO) consortium ocean model (Madec *et al.*, 2017). The NEMO ocean model, at a horizontal resolution of 0.25°, is comprised of 75 vertical levels, with eight model levels in the upper 10 m of the ocean. A 1-h coupling frequency is used in the coupled model to exchange information between the ocean–sea ice and atmosphere–land components. The ocean–sea ice and atmosphere–land components are initialised separately, with their own data assimilation (DA) systems. The coupled model uses the Forecast Ocean Assimilating Model (FOAM)–NEMOVAR DA system from Blockley *et al.* (2014) and Waters *et al.* (2015) to initialise its SST and sea-ice concentrations. The atmosphere–land component is initialised with the 4D-Var DA system (Rawlins *et al.*, 2007), which uses SST and sea-ice concentrations from the Operational Sea Surface Temperature and Ice Analysis (OSTIA: (Donlon *et al.*, 2012)) assimilation system, updated by Fiedler *et al.* (2019) and Good *et al.* (2020). More detailed model descriptions are available in section 2 of Vellinga *et al.* (2020).

### 2.2 | Experimental setup

To suppress the diurnal cycle of SST artificially in the NEMO ocean model, vertical eddy diffusivity was increased to a very large, unrealistic value ( $10 \text{ m}^2 \cdot \text{s}^{-2}$ ) over a specific mixing depth, such that the water column was instantaneously mixed over this mixing depth at each time step. Two mixing depths were chosen in this study, 5 m and 10 m, and the model runs for these mixing depths will be hereafter referred to as CPLDmix5m and CPLDmix10m, respectively. The control coupled and atmosphere-only models will be referred to as the CPLD and ATM models, respectively. The 5-m mixing depth was chosen because the typical e-folding depth of the observed

TABLE 1 Model specification summary.

Start date	End date	Atmosphere horizontal resolution	Atmosphere no. of levels in coupled (atmosphere-only) model	Ocean horizontal resolution	Ocean no. of levels	Global atmosphere (GA) version	Global land (GL) version	Global ocean (GO) version	Global sea-ice (GSI) version
May 1, 2016	Sep 24, 2018	N216	L85 (L70)	ORCA025	L75	GA6.1	GL6.1	GO5	GSI6
Sep 25, 2018	May 31, 2021	N320	L70 (L70)	eORCA025	L75	GA7.2	GL8.1	GO6.0	GSI8.0

References: GA6.1 and GL6.1 (Walters *et al.*, 2017); GA7.2, GA7.2.1, and GL8.1 (Walters *et al.*, 2019); GO5 (Megann *et al.*, 2014); GO6.0 (Storkey *et al.*, 2018); GSI6 (Rae *et al.*, 2015); GSI8.0 and GSI8.1 (Ridley *et al.*, 2018).

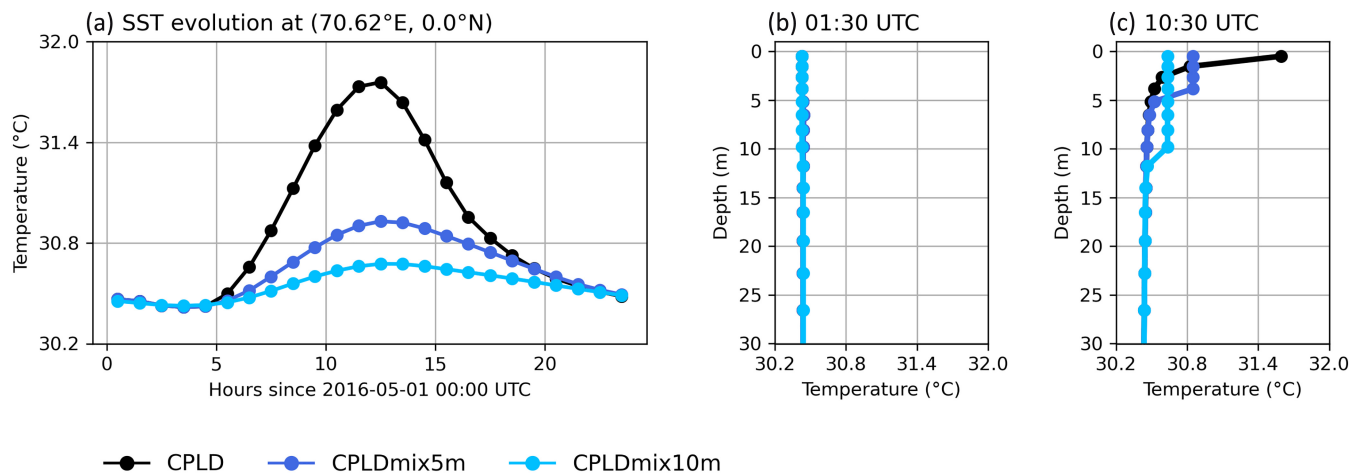


**FIGURE 1** Sample evolution of surface diurnal warm layer for one grid point in the Indian Ocean (70.625°E, 0°N) during the first 24 hours of the forecast initialised on May 1, 2016: (a) sea-surface temperature (SST), and the vertical profiles of ocean temperature at (b) 0130 UTC (0610 LST) and (c) 1030 UTC (1510 LST).

diurnal warm layers is 4–5 m (Matthews *et al.*, 2014). The 10-m mixing depth was selected for more direct comparisons of the coupled model with the ATM model, which uses bulk 10-m SSTs from the OSTIA dataset. Mixing depths deeper than 10 m were not considered for the experiments, as the entrainment of cold water from below the mixed layer in some regions, such as the MC, would lead to the daily mean SST being lower than the expected night-time SST in these regions (not shown).

An example evolution of the SST for a grid point in the Indian Ocean in the CPLD model and in the mixing experiments for the first 24 h of the forecast initialised on May 1, 2016 is displayed in Figure 1a. The additional mixing mutes the amplitude of the diurnal cycle of SST during this forecast. The maximum SST during this forecast is reduced by 0.8 °C in the CPLDmix5m model, and by >1 °C in the CPLDmix10m model run. The effect of the enhanced mixing on the near-surface temperature profiles can be seen in Figure 1b,c. During the night, for example, 0130 UTC in the Indian Ocean, any surface diurnal warm layer will have disappeared due to background mixing. Hence, the night-time temperature profiles are similar between the CPLD model and the mixing experiments (Figure 1b). During the afternoon (1030 UTC in the Indian Ocean), the CPLD model develops a strong diurnal warm layer (Figure 1c). However, in the instantaneous mixing experiments, the ocean temperature in the upper half of the mixing depth decreases compared with the CPLD model. In the lower half of the mixing depth, the ocean temperature increases compared with CPLD, such that the instantaneous mixing conserves the energy of the system and distributes it equally within the specified mixing depth. Therefore, the instantaneous mixing effectively degrades the vertical resolution of the ocean

model, creating a homogeneous top model layer of the same thickness as the mixing depth.

Salinity changes in the mixing experiments are of the order of 0.01 psu (not shown), similar in magnitude to the observed values of the diurnal cycle of salinity in the Tropics (Drushka *et al.*, 2014a). The equivalent density change for a 1 °C change in temperature requires a salinity change of 0.5 psu at a typical tropical SST (27 °C). Such a salinity change would impact barrier layers and mixing from below the mixed layer. The imposed mixing does not extend beyond the mixed layer in our experiments and the changes in the salinity are small. Therefore, the changes to salinity stratification due to the imposed mixing will not have a substantial effect on the SSTs in our experiments.

### 2.3 | Real-time multivariate MJO index

The Wheeler and Hendon (2004) real-time multivariate MJO index (RMM) is used to quantify the MJO performance (full methodology available in Gottschalck *et al.* (2010), with references therein). Daily anomalies of top-of-atmosphere outgoing longwave radiation (OLR) and zonal winds at 850 and 200 hPa are used to construct the index. The RMM1 and RMM2 indices are the principal component time series corresponding to the dominant spatial structures of the data. The RMM indices define the location of the MJO convection in the Tropics with eight phases. In phases 8 and 1, the MJO is located over the western hemisphere and Africa. During phases 2 and 3, the MJO convective anomalies propagate across the Indian Ocean, reaching the MC in phases 3 and 4. During phases 6 and 7, the MJO is located over the western Pacific. In

this study, days with an active MJO are defined as those for which the RMM amplitude  $\sqrt{\text{RMM1}^2 + \text{RMM2}^2} \geq 1.0$ .

Model indices are verified against the Wheeler–Hendon index Wheeler and Hendon (2004).<sup>1</sup> Four standard scalar statistics are used for model performance between the model indices and the Wheeler–Hendon indices, following Lin *et al.* (2008) and Rashid *et al.* (2011): bivariate anomaly correlation coefficient, root-mean-square error (RMSE), amplitude error, and phase error. The first two correspond to the spatial correlation between the models and the verification dataset. A skilful prediction is found for  $\text{RMSE} < \sqrt{2}$  and correlation  $> 0.5$  (Lin *et al.*, 2008). A negative (positive) amplitude error in the model signifies underestimated (overestimated) RMM amplitude. The phase error is the angle in degrees in RMM phase space and is positive (negative) when the MJO in the model is located to the east (to the west) of the verification dataset. The active MJO days between May 1, 2016 and May, 31 2021 for the boreal winter season (November–April) are used for each lead day to calculate the RMM statistics.

## 2.4 | Composites and observational datasets

Composite maps are calculated for daily means of meteorological variables regridded to N180 ( $1^\circ \times 1^\circ$ ) horizontal resolution. Separate forecast initialisations are concatenated at a given lead time for further processing. Anomalies are calculated by the removal of the seasonal cycle (annual mean and first three harmonics) for the period 2017–2020 at a given lead time. The MJO anomalies are then obtained by a temporal filtering of the anomalies with a 20–200 day bandpass Lanczos filter (Duchon, 1979) at each lead time. The composites are split by the initial MJO phase from the Wheeler–Hendon indices at lead day 1. Consecutive forecast initialisations with the same initial MJO phase are averaged before compositing and treated as one event. Unless otherwise stated, the initially active MJO forecasts during the November–April season are used for the composite analysis for the period November 1, 2016–January 15, 2021. The composites for daily interpolated OLR from the National Oceanic and Atmospheric Administration (NOAA) at  $2.5^\circ \times 2.5^\circ$  resolution (Liebmann & Smith, 1996) were calculated until January 7, 2021 based on the observed data availability. Mean state composites of all meteorological variables in Section 3.3 were calculated for the boreal winter period from November 1, 2016–January 15, 2021, including both active and non-active MJO days. Missing days (less than 1%) were interpolated between the nearest previous and next-day forecast initialisations.

## 3 | RESULTS

### 3.1 | MJO model performance and diurnal warming

In the following section, the overall MJO performance is discussed with the RMM skill statistics averaged across all MJO phases for the CPLD, CPLDmix5m, CPLDmix10m, and ATM models. The data used here span the boreal winter season and active MJO days only. Qualitatively, no significant difference in the RMM skill statistics was found for year-round data.

The CPLD, CPLDmix5m, CPLDmix10m, and ATM models predict the MJO skilfully out to 15 lead days, with the bivariate correlation coefficients above 0.70 at all times during the forecast (Figure 2a). There is little difference between the models in bivariate correlation coefficients, with the exception of the ATM model, which produces slightly smaller coefficients than the coupled model runs at lead day 15. All models are within the skilful RMSE threshold out to 15 forecast days (Figure 2b). The ATM model predicts slightly larger RMSE than the coupled runs from lead day 12 onward. At lead day 15, the RMSE for all models reaches close to the threshold for poor prediction, suggesting that at longer lead times these models may not be skilful in predicting the MJO. The RMM amplitude decreases in all models with lead time, reaching  $-0.25$  amplitude error by lead day 15 (Figure 2c). The coupled model runs show slightly better amplitude error than the ATM model from lead day 10 onward.

The largest difference between the models is recorded in the RMM phase error (Figure 2d). At lead day 1, all models predict the MJO to the east of the verification dataset, that is, too fast eastward propagation. Afterwards, the ATM model predicts the MJO to the west of the verification dataset (i.e., too slow eastward propagation) at  $-1.5^\circ$  phase error for lead days 3–6. At longer lead times, the ATM model phase error varies between  $-2.5^\circ$  and  $2.5^\circ$ , reaching  $-2.1^\circ$  at lead day 15. During the first seven lead days, the ATM model predicts the MJO with approximately correct phase speed, likely due to compensating biases present in the ATM model. At the same time, all coupled models simulate a too-fast MJO compared with the verification dataset. The phase errors for the CPLD, CPLDmix5m, and CPLDmix10m models evolve similarly within the first seven lead days of the forecast. However, the additional mixing in the upper ocean reduces the phase speed in CPLDmix5m and CPLDmix10m compared with the CPLD model, such that deeper mixing causes a stronger reduction in the MJO phase speed, and as a result a stronger reduction in the RMM phase error. This is particularly evident at lead days longer than 10, likely due to secondary

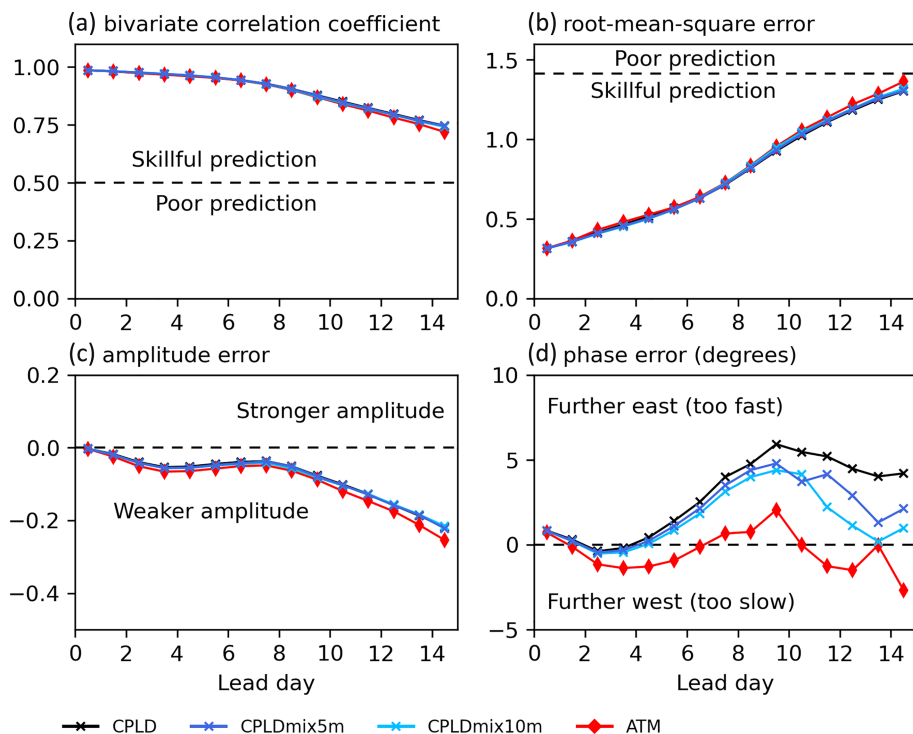


**FIGURE 2** Real-time multivariate Madden-Julian Oscillation (MJO) index skill statistics as a function of lead day for CPLD, CPLDmix5m, CPLDmix10m, and ATM models: (a) bivariate correlation coefficient; (b) root-mean-square error; (c) amplitude error; and (d) phase error. Daily mean data are compared for boreal winter season (November–April) and active MJO days only with the Wheeler–Hendon verification indices.

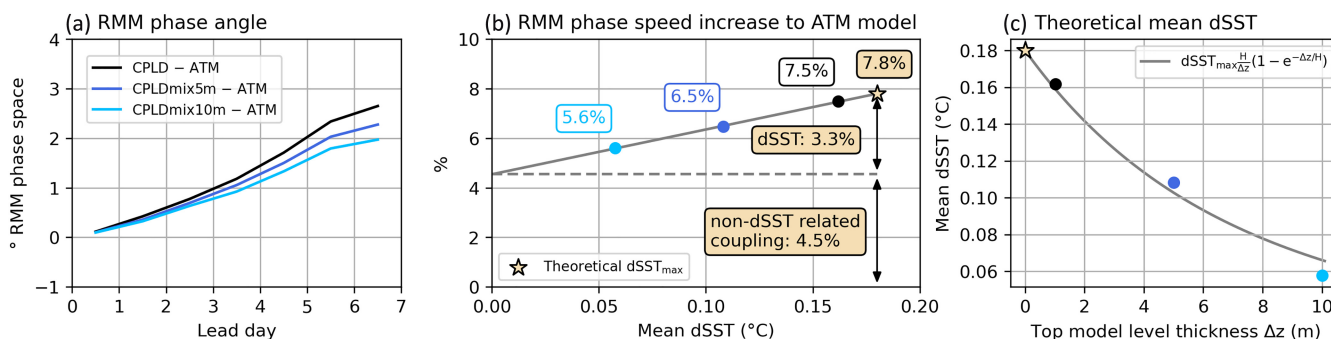


**FIGURE 3** (a) Real-time multivariate Madden-Julian Oscillation (RMM) phase-angle difference between the coupled model experiments (CPLD, CPLDmix5m, and CPLDmix10m) and the ATM model as a function of lead day; (b) RMM phase-speed increase (percent) between the coupled model experiments and the ATM model at lead day 7 of the forecast as a function of the mean diurnal warming of sea-surface temperatures (dSST, difference between the 1500 and 0600 local solar time sea-surface temperature) in the Tropics (30°S–30°N) at lead day 1 in the coupled model experiments; (c) best fit between the top model level thickness and the mean dSST in the Tropics at lead day 1 for  $dSST_{max} = 0.18^\circ\text{C}$  and  $H = 4.0\text{ m}$ .

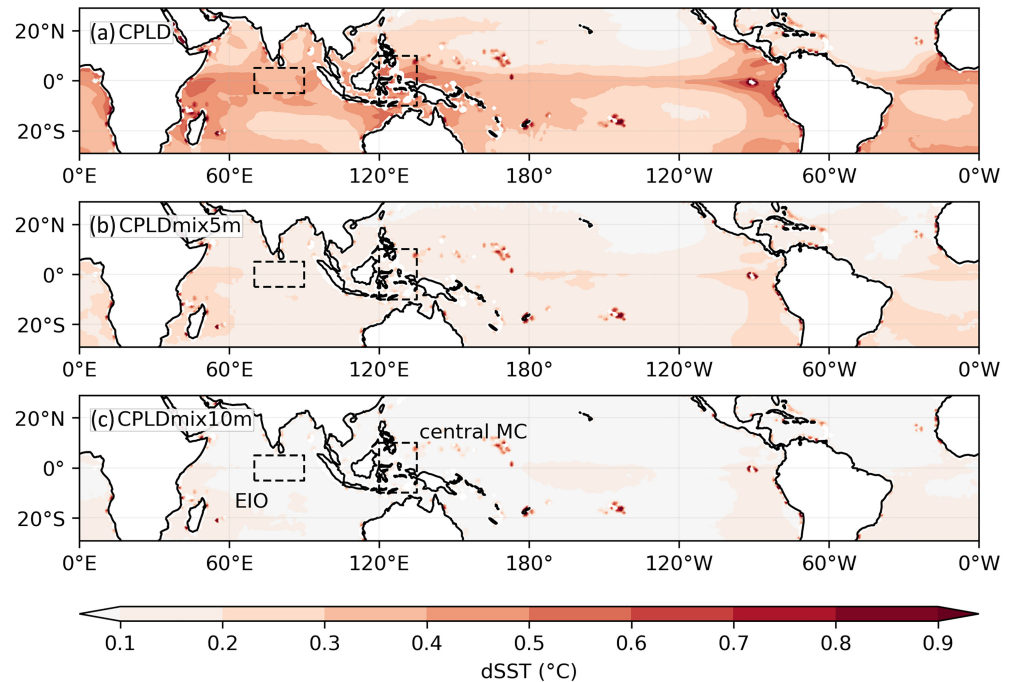
feedbacks between the ocean and the atmosphere. Those feedbacks are explored in Section 3.2.2.

All three coupled model runs show a linear growth in the RMM phase angle compared with the ATM model during the first seven lead days of the forecast (Figure 3a). The CPLD model displays the strongest increase in RMM phase angle compared with the ATM model, at a rate of  $0.44^\circ \cdot \text{d}^{-1}$  (in RMM phase space). The CPLDmix5m and CPLDmix10m models show a weaker increase in the RMM phase angle compared with the ATM model at  $0.38^\circ \cdot \text{d}^{-1}$  and  $40.33^\circ \cdot \text{d}^{-1}$  (RMM phase space), respectively. The average RMM phase speed during the study period in the ATM

model was  $5.9^\circ \cdot \text{d}^{-1}$  (RMM phase space). Therefore, the equivalent increase in RMM phase speed for the coupled runs compared with the ATM model stands at 7.5%, 6.5%, and 5.6% for the CPLD, CPLDmix5m, and CPLDmix10m models, respectively. This is lower than the 12% recorded by Karlovska *et al.* (2024) for a higher resolution version of the CPLD model, although they used the observed RMM phase speed in their comparison, which is slightly slower than the ATM model RMM phase speed. Qualitatively, the choice of ATM rather than OBS as a baseline makes little difference in the quoted values (e.g., 8.5% instead of 7.5% for the CPLD model). The exact increase in speed is



**FIGURE 4** Composite diurnal warming (dSST; 1500 minus 0600 local solar time SST difference) at lead day 1 for (a) CPLD, (b) CPLDmix5m and (c) CPLDmix10m averaged over all MJO phases (boreal winter and initially active MJO forecasts only). The boxes indicate where area averages are taken later over the equatorial Indian Ocean (EIO) and central Maritime Continent (MC).



likely to vary between models, but we expect the key finding to remain: coupling increases the speed of the MJO, and a substantial component of this speed-up is due to the representation of the diurnal cycle of SST.

To understand the increase in MJO phase speed in the coupled model further, it is important to understand the main differences between the models, that is, the nature of SSTs in each model. The ATM model utilises persisted SSTs from the OSTIA dataset that correspond to the bulk 10-m night-time ocean temperature. Therefore, this dataset does not include any diurnal warming effects on the SSTs, nor the air–sea interactions due to the diurnal cycle. The ocean component of the CPLD model is comprised of eight model levels in the top 10 m of the ocean and has the capacity to produce diurnal warm layers (Figure 1c, also see Karłowska *et al.* (2024) for diurnal warm-layer formation in the CPLD model). The CPLD model SSTs correspond to the top model level centred at 0.51 m, bounded by 0.0 and 1.02 m depth. The CPLDmix5m and CPLDmix10m model runs are a variation of the CPLD model run and are capable of developing diurnal warm layers, but with greatly reduced diurnal amplitude. The additional mixing reduces the amplitude of the diurnal warming in these model runs and increases the effective thickness of the SST layer from 1.0201 to 5 m and 10 m for the CPLDmix5m and CPLDmix10m models, respectively.

The boreal winter composite of active MJO days for the diurnal warming of SST (dSST), defined here as the difference between the 1500 and 0600 local solar time (LST) SST, is positive at lead day 1 in the CPLD model across the Tropics (Figure 4a). The strongest dSST is recorded

near the Equator, with mean values  $>0.4^{\circ}\text{C}$ . The dSST is largest in the western Indian Ocean, over the MC, and in the eastern Pacific. The mean dSST at lead day 1 in the Tropics ( $30^{\circ}\text{S}$ – $30^{\circ}\text{N}$ ) in the CPLD model stands at  $0.16^{\circ}\text{C}$ . The dSST in CPLDmix5m is reduced across the Tropics to a mean value of  $0.11^{\circ}\text{C}$  (Figure 4b). A further reduction in the mean tropical dSST is observed in the CPLDmix10m model, with values  $<0.1^{\circ}\text{C}$  across the majority of the Tropics and a mean value of  $0.06^{\circ}\text{C}$  (Figure 4c). The night-time tropical SST (at 0600 LST) does not vary substantially between all coupled experiments over 15 lead days of the forecast (Figure 5). The difference in night-time SST between the coupled experiments at lead day 15 is  $<0.01^{\circ}\text{C}$ . Therefore, the mixing experiments suppress the diurnal variations of SST successfully with minimal side effects on other processes, such as the evolution of the ocean mixed layer.

The percentage increase in the RMM phase speed between the coupled model runs and the ATM model out to lead day seven is linearly correlated with the mean dSST in the Tropics at lead day 1 in each coupled model run (Figure 3b). Theoretically, if the diurnal warming effects were removed from the CPLD model entirely (dSST =  $0^{\circ}\text{C}$ ), the intersect of the linear fit between the mean tropical dSST and the RMM phase-speed increase between the coupled models and the ATM model would correspond to all other coupling effects unrelated to dSST. Those effects would be present in all the coupled model runs, regardless of dSST strength.

Ignoring the cool skin effect, it is straightforward to calculate what the theoretical maximum of dSST in the

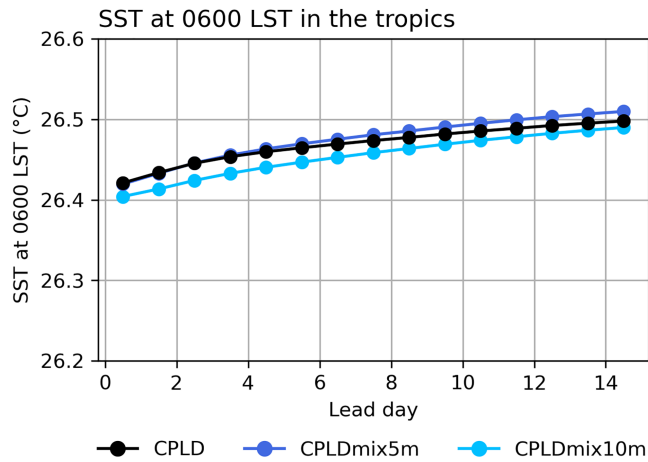


**FIGURE 5** Composite 0600 local solar time (LST) SST for CPLD, CPLDmix5m, and CPLDmix10m averaged over the Tropics (30°S–30°N), and over all MJO phases (boreal winter and initially active MJO forecasts only).

CPLD model would be as the thickness of the top model level decreases towards the skin depth of the water surface. Ocean glider observations of diurnal warm layers in the Indian Ocean show that the additional diurnal warming with respect to the foundation temperature at the base of the diurnal warm layer can be described by an exponential decay with depth, with a caveat that such decay is observed on days with sunny weather and weak surface winds and not during enhanced MJO convection (Matthews *et al.*, 2014). The bulk temperature profile  $T(z)$  with a superimposed diurnal warm layer can be described as

$$T(z) = T^* + \text{dSST}_{\max} e^{-z/H}, \quad (1)$$

where  $T^*$  is the foundation SST,  $\text{dSST}_{\max}$  is the theoretical maximum dSST, and  $H$  is the scale depth of the diurnal warm layer. The modelled surface temperature  $T_{\text{sfc}}$  is then a vertical average of this temperature profile for each model run over the SST layer thickness ( $\Delta z$ ):

$$\begin{aligned} T_{\text{sfc}} &= \frac{1}{\Delta z} \int_0^{\Delta z} T^* + \text{dSST}_{\max} e^{-z/H} dz \\ &= T^* + \text{dSST}_{\max} \frac{H}{\Delta z} (1 - e^{-\Delta z/H}). \end{aligned} \quad (2)$$

Therefore the theoretical dSST contribution to the surface temperature is

$$\text{dSST}(\Delta z) = \text{dSST}_{\max} \frac{H}{\Delta z} (1 - e^{-\Delta z/H}). \quad (3)$$

A least-squares regression was fitted to obtain the optimum  $\text{dSST}_{\max}$  and  $H$  for  $\Delta z$  and the mean tropical dSST in all coupled model runs (Figure 3c). The optimum  $\text{dSST}_{\max}$

and  $H$  were found at 0.18 °C and 4.0 m, close to the values recorded from observations collected by ocean gliders in the central Indian Ocean ( $\text{dSST}_{\max} = 0.22$  °C;  $H = 4.2$  m) by Matthews *et al.* (2014). Theoretically, the mean dSST would tend to the value of  $\text{dSST}_{\max}$  with increasing vertical ocean resolution. Therefore, the theoretical maximum MJO phase-speed increase in the CPLD model compared with the ATM model can be extrapolated to 7.8% for  $\text{dSST}_{\max} = 0.18$  °C (Figure 3b). This value is slightly larger than the value for the CPLD model at the current vertical resolution in the ocean model. This shows that the ~1 m vertical resolution in this coupled model is sufficient to capture almost all of the effects of the diurnal warm layer on the MJO and there is no need to increase this vertical resolution further.

On a seven-lead-day timescale, the presence of the dSST contributes approximately 40% of the MJO phase-speed increase between the CPLD and ATM models. The representation of the dSST is therefore important for the eastward propagation of the MJO in this coupled NWP system. The remaining 60% is contributed by other coupling effects unrelated to diurnal warming, for example, mixed-layer and barrier-layer contributions. The mixed layer in the coupled model at lead day 1 is deeper than the maximum depth of the imposed mixing in all coupled experiments across the Tropics at a mean value of ~30 m. The mixed-layer depth evolution throughout the forecast happens at the same rate in all coupled model runs (not shown), and hence the suppression of diurnal warming has a minimal effect on mixed-layer evolution in these experiments. The coupled model also simulates barrier layers; however, they are less than 10 m thick (not shown). Observations show that barrier layers larger than 10 m can increase the SST recovery after the MJO passage (Drushka *et al.*, 2014b; Moteki *et al.*, 2018). Therefore, barrier-layer contributions to the SST changes will be minor in this coupled model.

### 3.2 | MJO convection–diurnal warming–SST relationship

The mixing experiments show that muting the diurnal warming of SST (dSST) in the CPLD model can lead to a substantial reduction in MJO phase speed over a 15-lead-day forecast. In this section, we examine the relationship between MJO convection, dSST, and SST anomalies to investigate how a better representation of dSST leads to faster MJO propagation across different MJO phases in the CPLD model. The following section focuses on two regions that display the largest differences in MJO convection between the CPLD and the ATM models: the equatorial Indian Ocean region (EIO: 70°S–90°N, 5°S–5°N)

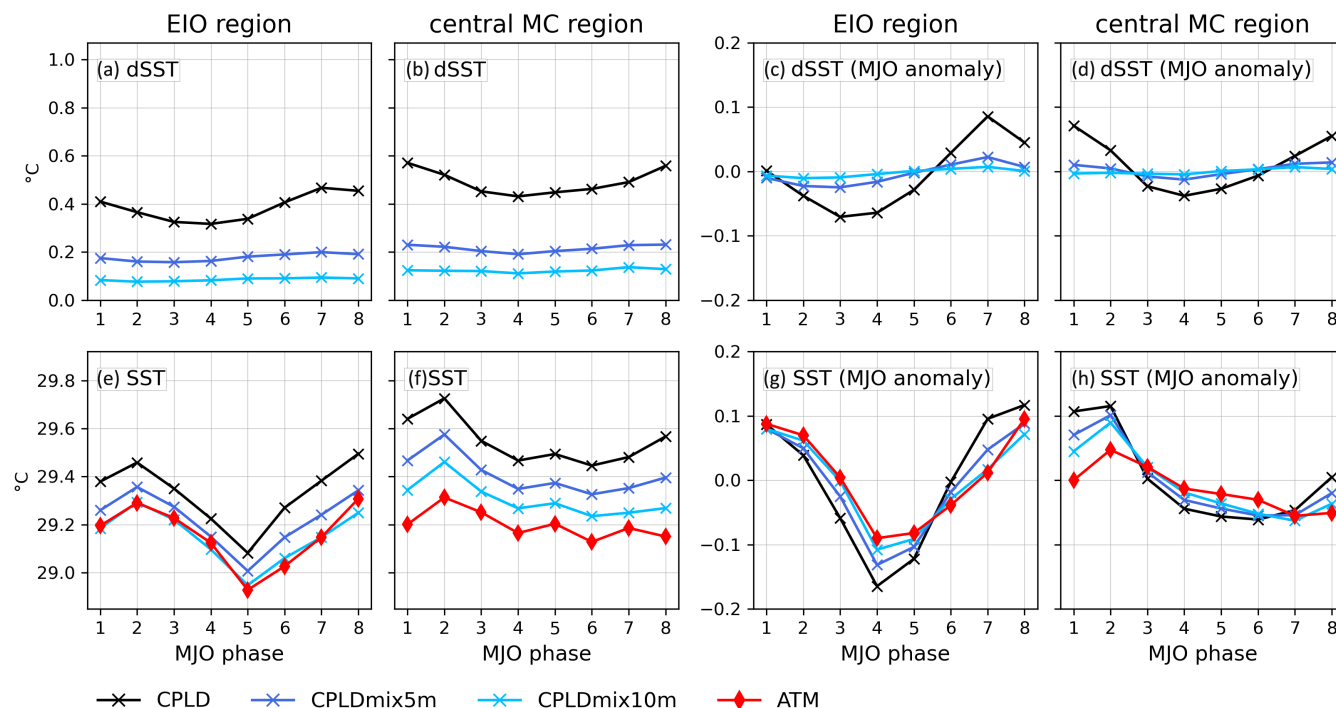


**FIGURE 6** Composite lead day 1 daily means for CPLD, CPLDmix5m, CPLDmix10m, and ATM models for (a,b) diurnal warming of SST (dSST; difference between 1500 and 0600 local solar time SST); (c,d) MJO anomalies of dSST (20–200 day filtered); (e,f) SST; (g,h) MJO anomalies of SST. The EIO and central MC regions are shown in Figure 4. Composites are calculated for boreal winter and initially active MJO forecasts only.

and the central MC region (120°S–135°N, 10°S–10°N). The spatial extent of these regions is displayed in Figure 4c.

### 3.2.1 | MJO impact on diurnal warming and daily mean SST

Karłowska *et al.* (2024) showed that the MJO conditions in a higher horizontal atmospheric resolution version of the CPLD model set the strength of the dSST. During suppressed MJO conditions, low surface winds and high shortwave (SW) flux into the ocean lead to stronger than average dSST in the coupled model. Conversely, during active MJO convection, cloud cover and stronger winds lead to weaker than average dSST. The same mechanism occurs in the lower horizontal atmosphere resolution version of the coupled model used in the experiments here. During initial MJO phases 6–1, the suppressed MJO convection over the EIO region (not shown) leads to stronger dSST than in phases 2–5 (Figure 6a), when MJO convection is enhanced. The same relationship between the dSST and MJO convection occurs in the central MC region (Figure 6b). The strongest dSST is recorded in initial MJO phases 7–2 during the suppressed MJO convection over the MC. During initial MJO phases 3–6, the MJO convection is located over the MC and thus the CPLD model generates a weaker dSST.

The CPLD model dSST at lead day 1 varies in each region between 0.3 and 0.6 °C across different MJO phases (Figure 6a,b). Both mixing experiments show a reduction in dSST in each region to ~0.2 and ~0.1 °C for the CPLDmix5m and CPLDmix10m models, respectively. Both mixing experiments also show a smaller phase-to-phase variation in the dSST than the CPLD model. Muted dSST in the coupled model at lead day 1 leads to a reduction in the lead day 1 daily mean SST in each region (Figure 6e,f, as colder water is mixed up to the surface as in Figure 1c). The additional mixing in the CPLDmix5m model leads to a 0.1–0.2 °C reduction in the daily mean SST in both regions across different initial MJO phases. The CPLDmix10m model displays a further reduction in the daily mean SST of 0.05–0.1 °C compared with the CPLDmix5m model daily mean SST. The reduction in the daily mean SST in the mixing experiments corresponds to approximately half of the reduction in the dSST. The CPLDmix10m effectively degrades the CPLD model to a 10-m top level, such that the reduction in the dSST causes the SSTs to cool down systematically towards the foundation SST at lead day 1 (Figure 6e,f).<sup>2</sup> Overall, the presence of the dSST in the CPLD model leads to an increase in the daily mean SST compared with the ATM model, which uses foundation SST and does not resolve the diurnal warming effects.

Diurnal warm layers form during the day and are destroyed overnight due to the night-time heat loss. After



removal of the mean, and subsequent 20–200-day band-pass filtering, the dSST anomalies are hereafter referred to as “MJO anomalies.” Non-zero MJO anomalies of dSST emerge in the CPLD model at lead day 1 in both regions across different MJO phases, as a result of the systematic modulation of dSST by the MJO (Figure 6c,d). During suppressed MJO conditions, the CPLD model produces positive MJO anomalies of dSST, and during enhanced MJO convection the CPLD model simulates negative MJO anomalies of dSST. The MJO anomalies of dSST in the CPLDmix5m model are reduced compared with the CPLD model, however, with a similar, but much reduced, phase-to-phase variation in the amplitude. The CPLDmix10m MJO anomalies of dSST are reduced further, being below  $0.02^{\circ}\text{C}$  across all initial MJO phases. The MJO anomalies of SST between the models reflect the behaviour seen in the MJO anomalies of the dSST (Figure 6g,h and c,d). More positive (negative) MJO anomalies of dSST lead to stronger positive (negative) MJO anomalies of SST in the coupled model. Moreover, the strong reduction in the MJO anomalies of dSST in the CPLDmix10m model yields MJO anomalies of SST that are closer in value to the ATM model MJO anomalies of SST, especially in the EIO region (Figure 6g). The additional mixing in the central MC region reduces the MJO anomalies of SST in the

coupled model towards those of the ATM model, except in phases 1 and 2, where a difference of around  $0.1^{\circ}\text{C}$  remains (Figure 6h).

Thus, the dSST in the CPLD model is modulated by the MJO conditions. The dSST then rectifies the daily mean SST and the daily mean MJO anomalies of SST. This mechanism, hypothesised by Karlovska *et al.* (2024), is confirmed by the mixing experiments carried out in this study. We now consider how the relationship between the MJO, the dSST, and the SST manifests over 15 lead days of the forecast to yield a faster MJO in the dSST-resolving coupled model.

### 3.2.2 | Two-way feedback between the MJO and diurnal warm layers

In this section, two initial MJO phases, 1 and 4, were chosen to describe the relationship between the MJO, the diurnal warming, and the SST in the CPLD model over 15 lead days of the forecast.

In initial MJO phase 1, the observations show negative MJO anomalies of OLR (enhanced MJO convection) over the Indian Ocean and positive MJO anomalies of OLR (suppressed MJO convection) over the MC (Figure 7a).

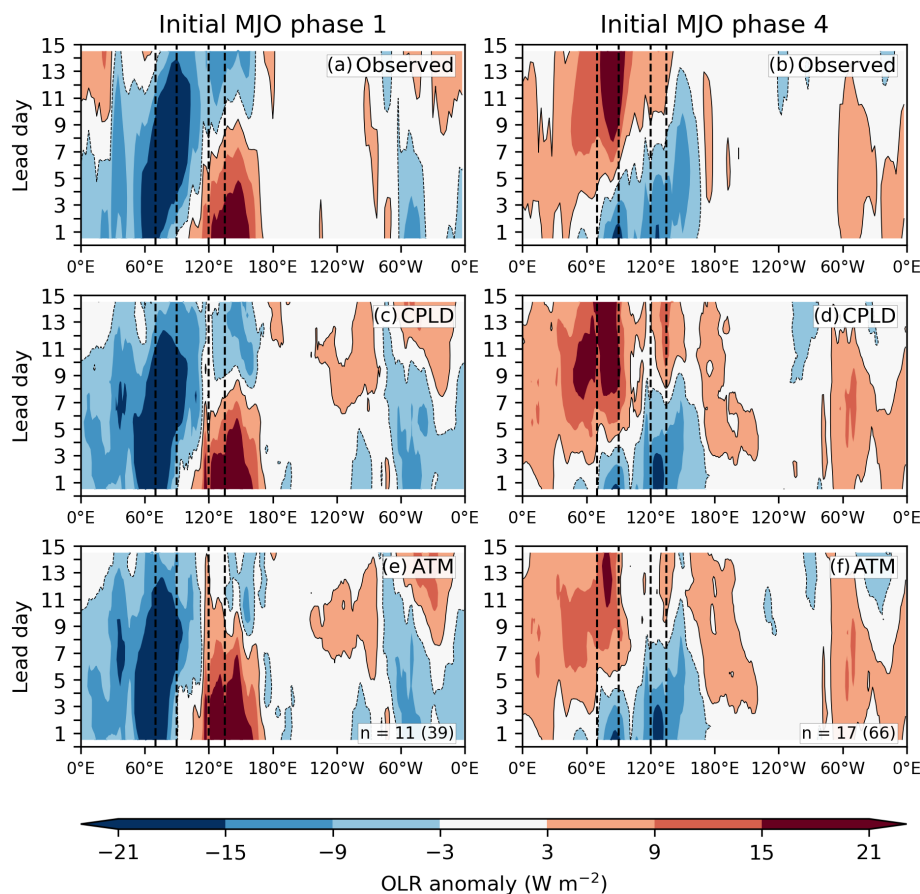
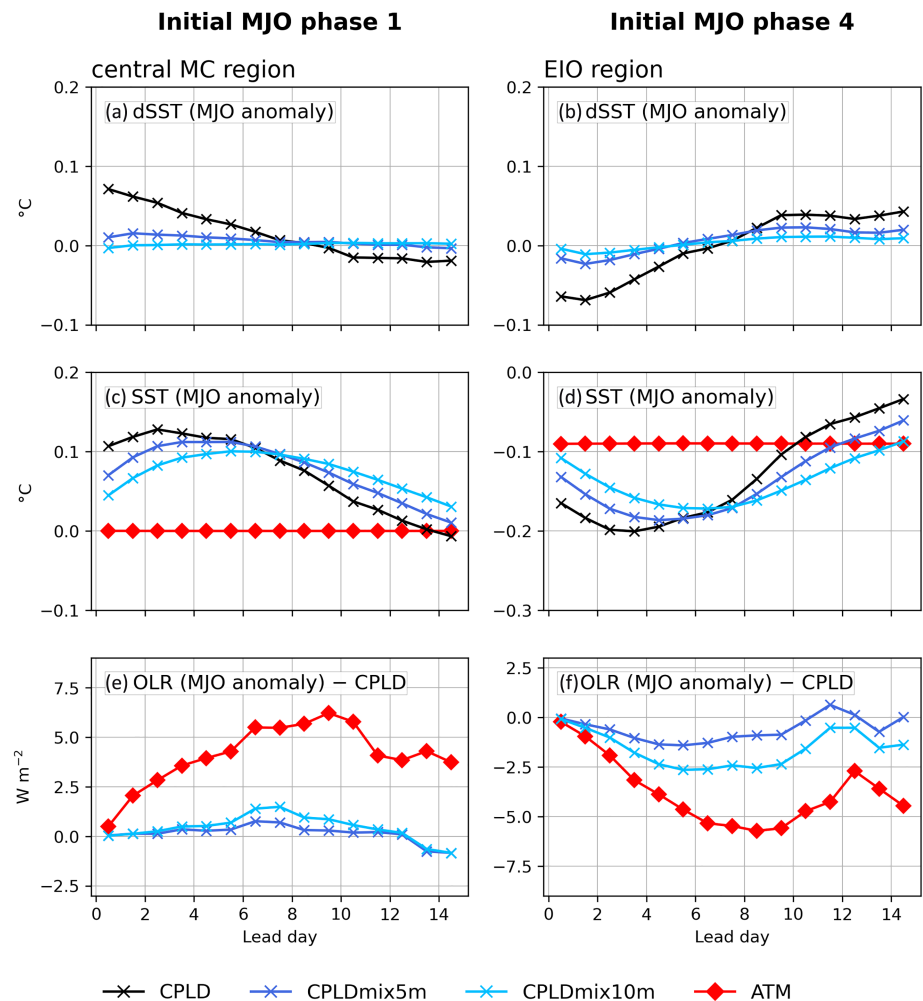


**FIGURE 7** Hovmöller diagrams of daily mean composites of MJO anomalous (20–200 day filtered) OLR, averaged over the equatorial band ( $5^{\circ}\text{S}$ – $5^{\circ}\text{N}$ ), for forecasts initialised in MJO phases 1 and 4: (a,b) observed; (c,d) CPLD model; (e,f) ATM model. Vertical dashed lines represent equatorial Indian Ocean and central Maritime Continent regions. Composites were calculated using boreal winter and initially active MJO forecasts only. Number  $n$  denotes the amount of independent events used in the composite (total number of days used displayed in brackets). Solid contours for positive values and dashed contours for negative values.

**FIGURE 8** Daily evolution of the model composites of MJO (20–200 day filtered) anomalies of (a,b) dSST; (c,d) SST; (e,f) OLR (difference from the CPLD model). (a,c,e) are for the central MC region for initial MJO phase 1; (b,d,f) are for the equatorial Indian Ocean (EIO) region for initial MJO phase 4. Composites are calculated for boreal winter for active MJO days only. The spatial extent of both regions is shown in Figure 4.



Both the CPLD and the ATM models simulate this pattern well (Figure 7b,e). The CPLD model simulates the onset of the MJO convection over the MC better than the ATM model at lead days 7 and beyond. The suppressed MJO convection over the MC leads to positive MJO anomalies of dSST in the central MC region (Figure 8a). The positive MJO anomalies of dSST in all coupled models lead to stronger positive MJO anomalies of SST compared with the ATM model (Figure 8c). The CPLDmix5m and CPLDmix10m MJO anomalies of SST at lead day 1 are reduced compared with the CPLD model SST due to the reduction in the MJO anomalies of dSST. The initially positive MJO anomalies of SST in all coupled models grow, peaking 3, 5, and 7 days later for the CPLD, CPLDmix5m, and CPLDmix10m models, respectively. The early arrival of the MJO anomaly of SST occurs due to the addition of diurnal warming on top of the canonical evolution of the MJO anomalies of SST due to the changes in net heat flux into the ocean ( $Q_{\text{net}}$ ) throughout the life cycle of the MJO. In the absence of diurnal warming in the CPLDmix10m model, the MJO anomalies of SST peak around lead day 7 when the MJO anomaly of  $Q_{\text{net}}$  is close to zero (not shown). The presence of strong MJO anomalies of dSST in the

CPLD model adds an extra, time-varying component to the MJO anomalies of SST, such that the CPLD model displays an earlier peak in positive MJO anomalies of SST in this region compared with the CPLDmix5m and CPLDmix10m models.

By lead day 7, the active MJO convection propagates into the central MC region (Figure 7a). Accordingly, the positive MJO anomalies of dSST weaken with lead day in each coupled model run, until lead day 7, when all models display MJO anomalies of dSST close to zero (Figure 8a). The difference in the MJO anomalies of SST between the CPLD model and the mixing experiments is small during this time of weakest dSST (Figure 8c). By lead day 7, the MJO convection differences between the CPLD and mixing experiments reach a maximum in response to the differences in MJO SST anomalies over the preceding days (Figure 8e). The MJO convection reaches the MC by lead day 7 (Figure 7a) and, accordingly, the dSST regime shifts to negative MJO anomalies of dSST growing past lead day 7 (Figure 8a).

The CPLD model displays the strongest decline in the MJO anomaly of SST compared with the mixing experiments, due to the strongest negative MJO anomalies of

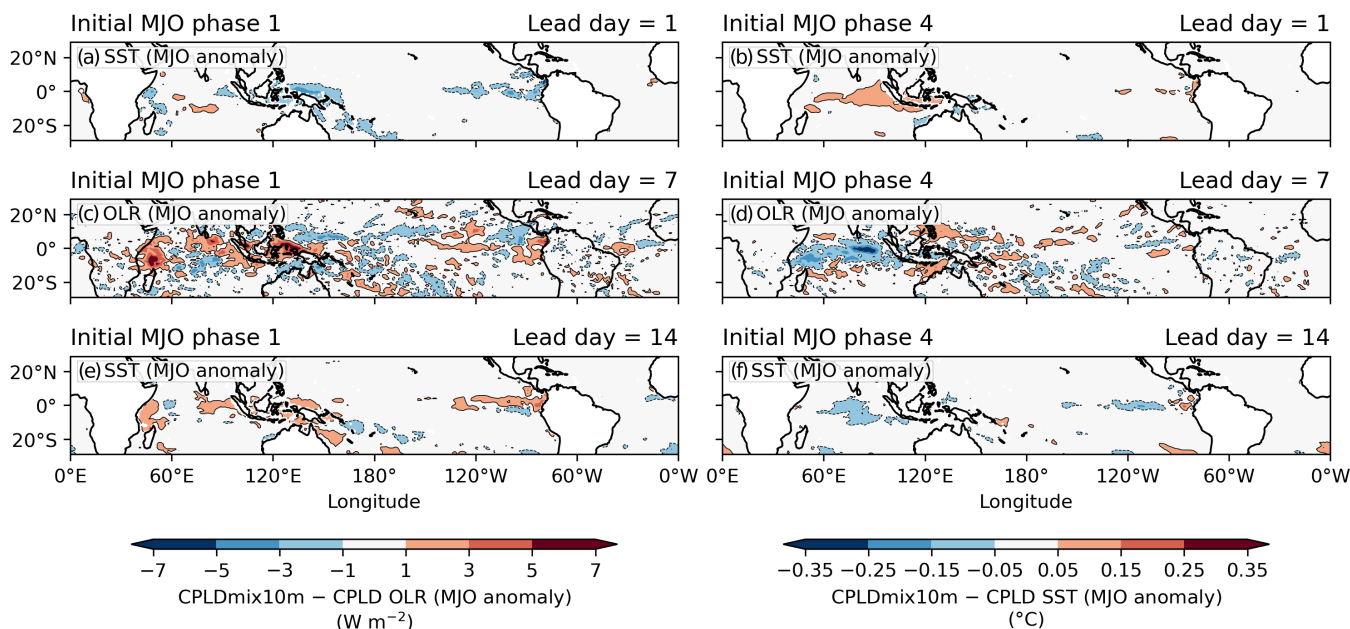


**FIGURE 9** Composite daily mean MJO (20–200 day filtered) anomalies of CPLDmix10m minus CPLD difference for (a,b) SST at lead day 1; (c,d) OLR at lead day 7; (e,f) SST at lead day 14. (a,c,e) are for initial MJO phase 1, (b,d,f) are for initial MJO phase 4. Composites are calculated from boreal winter data. Solid contours for positive values and dashed contours for negative values.

dSST. This decline takes approximately three lead days (from lead days 7–10). Afterwards, all coupled-model MJO anomalies of SST evolve in parallel to each other. This is a spatially coherent pattern in the coupled model. Colder MJO anomalies of SST over the MC at lead day 1 (Figure 9a) lead to less convection at lead day 7 in the CPLDmix10m model compared with the CPLD model (Figure 9c) during the convective MJO phase in that region (Figure 7c). The MJO anomalies of SST respond quickly to that change in the MJO convection, and, by lead day 14, less convection in the CPLDmix10m model leads to warmer MJO anomalies of SST compared with the control (Figure 9e).

In initial MJO phase 4 at lead day 1, the enhanced MJO convection spans most of the eastern Indian Ocean and the MC (Figure 7b). Both the CPLD and the ATM models reproduce this MJO convection well across the Tropics (Figure 7d,f). However, at longer lead days, the CPLD model overestimates the suppressed MJO convection over the western Indian Ocean. At the same time, the ATM model underestimates the suppressed MJO convection over the MC. The enhanced convection over the Indian Ocean leads to negative MJO anomalies of dSST in the CPLD model in the EIO region in MJO phase 4 at lead day 1 (Figure 8b). The mixing experiments show smaller, albeit still negative, MJO anomalies of dSST in this region at lead day 1. The stronger the MJO anomalies of dSST, the more negative the MJO anomaly of SST that is generated in the coupled model (Figure 8d). The negative MJO

anomalies of SST at lead day 1 grow in the coupled model runs, peaking 3, 5, and 7 days later for the CPLD, CPLDmix5m, and CPLDmix10m models, respectively. Similarly to the positive anomalies in Figure 8c, the negative MJO anomalies of SST in the EIO region grow by a similar increment between the coupled model runs each lead day until they reach their negative peak. The earlier arrival of negative MJO anomalies of SST in the CPLD model is associated with the stronger negative peak in the MJO anomaly of dSST that is superimposed on the MJO anomalies of SST seen in the CPLDmix10m simulation in the absence of diurnal warming.

As the forecast reaches lead day 7, the approaching suppressed MJO convection (Figure 7d) over the EIO region leads to a weaker negative MJO anomaly of dSST, reaching close to zero for all models at lead day 7 (Figure 8b). Consequently, during the weakest MJO anomaly of dSST at lead day 7, the MJO anomalies of SST in all coupled model runs are the closest to each other throughout the forecast (Figure 8d). At the same time, the difference in MJO convection between the mixing experiments and the CPLD model peaks (Figure 8f). That difference is larger when deeper mixing is imposed. The MJO anomalies of SST in the EIO region for initial MJO phase 4 recover from the MJO passage after lead day 7, and display a warming trend towards the end of the forecast (Figure 8d). The CPLD MJO anomalies of SST recover fastest between lead days 7 and 11 compared with the mixing experiments. Afterwards, all coupled-model MJO

anomalies of SST evolve in parallel to each other until day 15.

The spatial extent of this feedback can be seen in Figure 9b,d,f. The additional mixing in CPLDmix10m reduces the negative MJO anomalies of SST over the Indian Ocean compared with the CPLD model, leading to a positive SST difference (Figure 9b). By lead day 7, an organised enhanced MJO convection response is observed in the CPLDmix10m model in response to the warmer SSTs compared with the control over the preceding days. At lead day 7, the CPLDmix10m model simulates more convection over the central Indian Ocean compared with the CPLD model (Figure 9d) during the suppressed MJO phase (Figure 7d). By lead day 14, the CPLDmix10m model generates colder MJO SST anomalies compared with the CPLD model, due to the relatively enhanced MJO convection at lead day 7 in the CPLDmix10m model (Figure 9d).

The mechanism described in this section is a two-way feedback between the MJO convection and diurnal warm layers. At lead day 1, the MJO conditions in the coupled model dictate the strength of the dSST. The dSST rectifies the daily mean SST and daily mean MJO anomalies of SST. The addition of diurnal warming shifts the peak of the MJO anomalies of SST earlier in the forecast, and, by lead day 7, there is a coherent response in the MJO convection in the coupled model to the preceding MJO anomalies of SST. That convection has an instantaneous effect on the dSST, and within the next three lead days the MJO anomalies of SSTs respond to that convection change. The stronger the MJO anomalies of dSST in the coupled model, the faster the MJO anomalies of SST recover after the MJO transition from active to suppressed phase, and vice versa. Ultimately, more extreme anomalies of dSST in the coupled model lead to faster MJO phase speed, through the modulation of the convection via MJO anomalies of SST.

### 3.3 | Diurnal warming effect on the mean state

Analyses of NWP and climate models show that a steeper background horizontal moisture gradient results in improved eastward propagation of the MJO across the MC (Ahn *et al.*, 2020; Lim *et al.*, 2018). The key process in simulating a realistic MJO eastward propagation is the existence of a realistic background moisture distribution and the advection of this by the MJO winds (e.g., Jiang, 2017). NWP models that are prone to the development of dry mean-state biases in the lower troposphere over the Indo-Pacific warm pool tend to produce a reduced mean horizontal moisture gradient and display a poorer

MJO prediction skill (Kim *et al.*, 2019). Observations show that the presence of diurnal warming of SST (dSST) can increase the latent heat (LH) flux into the atmosphere by approximately  $4 \text{ W} \cdot \text{m}^{-2}$  (Fairall *et al.*, 1996; Matthews *et al.*, 2014). This increase can lead to changes in the mean state of the model and have subsequent effects on the MJO. Therefore, to understand the effect of the dSST on the mean state and the MJO, in this section we analyse the evolution of mean-state composite meteorological variables for six boreal winters in the warm-pool region ( $40^{\circ}\text{E}$ – $180^{\circ}\text{E}$ ,  $10^{\circ}\text{S}$ – $10^{\circ}\text{N}$ ) between November 1, 2016 and January 15, 2021 for the CPLD, CPLDmix5m, and CPLDmix10m models.

Muted dSST leads to cooler mean-state SST in the mixing experiments compared with the CPLD model over the warm-pool region (Figure 10a). The cooling decreases from lead day 1 to lead day 15, starting at  $-0.1^{\circ}\text{C}$  and  $-0.16^{\circ}\text{C}$  for the CPLDmix5m and CPLDmix10m models at lead day 1 and reaching  $-0.05^{\circ}\text{C}$  and  $-0.12^{\circ}\text{C}$  for these models by lead day 15. The lead day 1 mean-state SST difference between the mixing experiments and the CPLD model is reflected in the the upward LH flux into the atmosphere at lead day 1 (Figure 10b). Increased mixing in the upper ocean leads to cooler SSTs. Cooler SSTs will generally lead to less evaporation into the atmosphere, and hence lower LH flux is observed in the mixing experiments compared with the CPLD model. The pattern of the difference in the mean-state SST and the difference in the mean-state LH flux between mixing experiments and the CPLD model is spatially correlated with 0.95 correlation coefficient (not shown).

The mean-state downward shortwave (SW) flux at the surface at lead day 1 is similar between all coupled model runs (Figure 10c). At longer lead times, convection is suppressed in response to the cooler SSTs, such that the mixing experiments display more SW flux into the ocean compared with the CPLD model, reaching  $1 \text{ W} \cdot \text{m}^{-2}$  and  $2 \text{ W} \cdot \text{m}^{-2}$  difference by lead day 7 for the CPLDmix5m and CPLDmix10m models, respectively. The downward net heat flux,  $Q_{\text{net}}$ , shows a positive difference of  $\sim 5 \text{ W} \cdot \text{m}^{-2}$  at lead day 1 between the CPLDmix10m and CPLD models (Figure 10d). The majority of the  $Q_{\text{net}}$  difference in the warm-pool region is due to the SW and LH fluxes. The  $Q_{\text{net}}$  difference between the models gets smaller with lead day, due to a decreasing difference in the LH flux and an increase in the positive SW flux difference.

The mean-state difference in OLR evolves similarly to the SW flux difference, with less convection in the warm-pool region by lead day 7 in both mixing experiments compared with the control (Figure 10f). The difference in OLR is approximately the same as the SW flux difference. The mean state 10-m wind speed weakens steadily during the forecast, until lead day 9–10 when it reaches



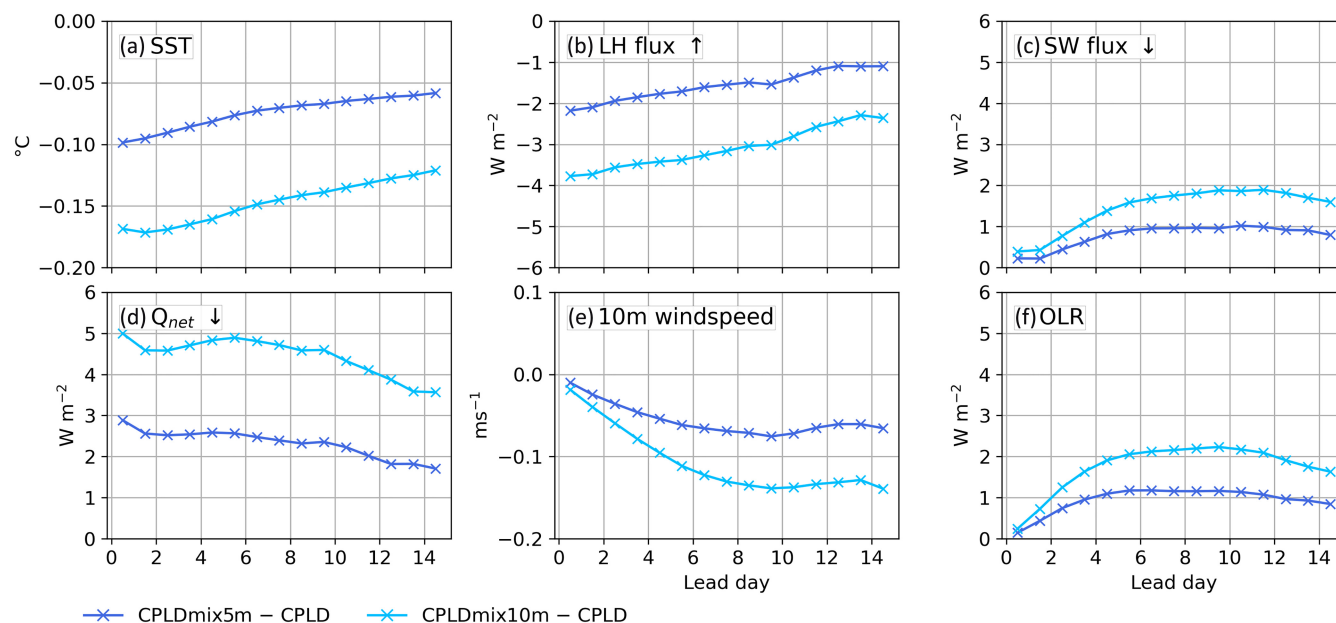


**FIGURE 10** Daily average difference for the mean-state composites in the warm-pool region ( $40^{\circ}\text{E}$ – $180^{\circ}\text{E}$ ,  $10^{\circ}\text{S}$ – $10^{\circ}\text{N}$ ) between the mixing experiments (CPLDmix5m and CPLDmix10m) and the CPLD model, for (a) SST; (b) upward latent heat flux into the atmosphere (LH flux); (c) downward shortwave flux into the ocean (SW flux); (d) downward net heat flux into the ocean  $Q_{\text{net}}$ ; (e) 10-m wind speed; (f) OLR. Composites are calculated with boreal winter season data only. Surface variables (SST, heat fluxes, and 10-m wind speed) are composite averages for sea grid points only.

approximately  $-0.07 \text{ m s}^{-1}$  and  $-0.14 \text{ m s}^{-1}$  difference for the CPLDmix5m and CPLDmix10m models, respectively (Figure 10e). This corresponds to weaker 10-m wind speed by 1.2% and 2.6% in the CPLDmix5m and CPLDmix10m models, respectively. The similar evolution in time of the wind speed and OLR differences suggests that the weaker wind speeds in the mixing experiments are due to the weakening of the Walker circulation.

The mean-state precipitation rate at the surface at lead day 1 is similar between all coupled model runs (Figure 11a). Both mixing experiments display a steady decline in the surface precipitation rate compared with the CPLD model until lead day 7. At lead day 7, the difference between the mixing experiments and the CPLD model reaches approximately  $-0.12 \text{ mm} \cdot \text{d}^{-1}$  and  $-0.25 \text{ mm} \cdot \text{d}^{-1}$  for the CPLDmix5m and CPLDmix10m models, respectively, and stays steady until lead day 15. At lead day 15, the majority of the warm-pool region in the mixing experiments displays a smaller surface precipitation rate than the CPLD model (Figure 11b,c). The strongest decrease in surface precipitation rate between the mixing experiments and the CPLD model at lead day 15 is approximately  $2 \text{ mm} \cdot \text{d}^{-1}$  and is located west of Sumatra and east of New Guinea. Biases of such magnitude over the warm-pool region can be linked to weaker moisture advection in NWP models, and ultimately weaker RMM amplitude (Kim *et al.*, 2019). A drier mean-state

lower troposphere in the CPLDmix10m model would indicate less background moisture, and might be expected to lead to a weaker MJO amplitude (Kim *et al.*, 2019). However, all coupled models investigated here display a very similar MJO amplitude over the 15 lead days of the forecast (Figure 2c). We hypothesise that, on a 15-lead-day timescale in this coupled NWP model, it is unlikely that there are substantial changes to the strength of the MJO due to diurnal warming effects on the low level background moisture.

In summary, the mean-state changes resulting from the suppression of the diurnal cycle of SST represent a weakening of convection and associated circulation patterns, and weaker surface precipitation linked to reduced evaporation at the sea surface. On a 15-lead-day timescale, these mean-state differences do not seem to affect the MJO amplitude in the coupled model. A stronger Walker circulation has been hypothesised to decelerate the MJO (Suematsu & Miura, 2022). All coupled models investigated here display a deceleration in the MJO phase speed from lead day 10, with the strongest deceleration recorded by the CPLDmix10m model (Figure 2d). In contrast to the results of Suematsu and Miura (2022), CPLDmix10m simulates the weakest Walker circulation and the strongest deceleration of the MJO past lead day 10. Further study is necessary, beyond the scope of this article, to separate the effects of the diurnal warm layer on the MJO

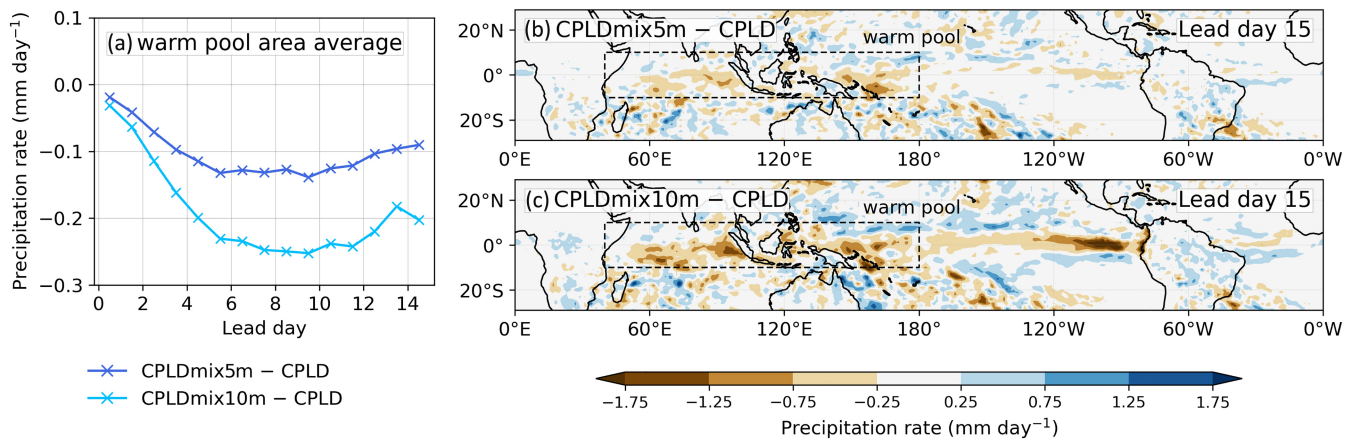


**FIGURE 11** (a) Daily average mean-state composite difference in surface precipitation rate over the warm-pool region ( $40^{\circ}\text{E}$ – $180^{\circ}\text{E}$ ,  $10^{\circ}\text{S}$ – $10^{\circ}\text{N}$ ) for CPLDmix5m minus CPLD and CPLDmix10m minus CPLD models; daily average mean state composite difference in surface precipitation rate at lead day 15 for (b) CPLDmix5m minus CPLD and (c) CPLDmix10m minus CPLD models. Composites are calculated with boreal winter season data only. Warm-pool extent is shown in (b) and (c).

and on the mean state–MJO relationship in this coupled model.

## 4 | DISCUSSION AND CONCLUSIONS

Hindcast experiments of the coupled ocean–atmosphere and atmosphere-only NWP models of the UK Met Office reveal skilful MJO predictions out to 15 lead days. The coupled model predicts a faster MJO than the atmosphere-only model, consistent with a previous study of Karlowka *et al.* (2024) that analysed higher horizontal atmospheric resolution versions of these models. They hypothesised that the addition of the diurnal warming of SST (dSST) in the coupled model, compared with the atmosphere-only model, leads to stronger MJO anomalies<sup>3</sup> of SST, and ultimately to a faster MJO. They proposed that stronger positive MJO anomalies of SST encourage MJO convection ahead of the MJO, while stronger negative MJO anomalies of SST behind the MJO inhibit MJO convection to the west. Using experiments that imposed instantaneous mixing in the upper few metres of the ocean, we reveal that this feedback does indeed lead to a faster MJO in the coupled NWP system of the UK Met Office. Reduction in the dSST leads to a reduction in the daily mean MJO anomalies of SST and those SSTs lead to differences in MJO convection, slowing the MJO down over 15 lead days during the forecast.

The increase in MJO phase speed in the coupled model compared with the atmosphere-only model over the first seven lead days of the forecast is related to the mean tropical dSST in the coupled model. The stronger the mean dSST that is produced in the coupled model at lead day

1, the larger the increase in MJO phase speed that is observed over the next seven days. On a seven-lead-day timescale, representing the tropical dSST in the coupled model increases the MJO phase speed by  $\sim 3\%$  relative to the atmosphere-only model. Coupling processes unrelated to the dSST contribute a further  $\sim 5\%$  phase speed increase, resulting in a  $\sim 8\%$  faster MJO phase speed in the coupled model compared with the atmosphere-only model. Karlowka *et al.* (2024) reported a larger, 12%, increase in MJO phase speed between these models at higher horizontal atmospheric resolution. The mean tropical dSST, however, does not differ substantially between the different versions of the coupled model, with a mean difference of  $<0.0002^{\circ}\text{C}$  (not shown). It is likely that the coupled NWP system of the UK Met Office is more sensitive to SST variability at a higher atmospheric horizontal resolution, or that the MJO speed increase unrelated to the dSST increases in this model with a higher horizontal resolution of the atmosphere component. Hence, about half of the MJO phase-speed increase in this coupled model, compared with the atmosphere-only version of the model on a seven-lead-day timescale, can be attributed to the dSST, and the other half to other coupling processes. While the proportion of the phase-speed increase due to dSST may differ in the observed MJO, it is worth noting that coupled models that struggle with the eastward propagation of the MJO may improve their skill by increasing the near-surface vertical resolution in the ocean model.

Diurnal warming of the ocean on calm, sunny days can be characterised by an exponential decay over the top few metres of the ocean (Matthews *et al.*, 2014). The coupled NWP model of the UK Met Office simulates that exponential decay. The mean tropical dSST in the coupled model decreases with increasing effective top model

layer thickness. Theoretically, we estimate that the maximum dSST in the coupled model in the Tropics at lead day 1 stands at  $0.18^{\circ}\text{C}$ , close to the observed value in the Indian Ocean reported by Matthews *et al.* (2014) of  $0.22^{\circ}\text{C}$ . The scaling depth of the exponential decay is found to be 4 m, very similar to the 4.2-m value observed in the Indian Ocean (Matthews *et al.*, 2014). At the current vertical resolution in the ocean component of the coupled model (approximately 1 m near the surface), the mean tropical dSST is close to the theoretical maximum at  $0.16^{\circ}\text{C}$ . The small difference between these two values suggests that little can be gained towards a better representation of the dSST in this coupled model should the near-surface vertical resolution be increased further. Additionally, the similarity of the spatial pattern of the dSST from Figure 4a to the spatial patterns of dSST from the reanalysis data validated with surface drifters for the 1979–2002 period from Bellenger and Duvel (2009) suggests that this coupled model simulates realistic diurnal warm layers. However, we conclude that models with a coarser vertical resolution in the near-surface ocean (of the order of 10 m, as is often used in climate models) may benefit from the parameterisation of diurnal warm layers.

The mixing experiments presented in this study provide an insight into the timescale and magnitude of the two-way feedback between the MJO and the dSST. The MJO conditions alter the strength of the dSST in the coupled model, such that stronger dSST is observed during suppressed MJO conditions, consistent with observations (Anderson *et al.*, 1996; Bellenger & Duvel, 2009; Itterly *et al.*, 2021; Matthews *et al.*, 2014). At lead day 1, the presence of the dSST increases the daily mean SST in the coupled model compared with the foundation SST used by the atmosphere-only model. The magnitude of the dSST and the resultant daily mean SST increase vary systematically with MJO phase, resulting in MJO anomalies in dSST that are positive (negative) in suppressed (active) convective conditions. The dSST then rectifies the MJO anomalies of SST in the coupled model, such that stronger MJO anomalies of dSST lead to stronger MJO anomalies of SST. Observations show that the dSST rectifies onto the intraseasonal SSTs (Itterly *et al.*, 2021; Yan *et al.*, 2021), and this coupled NWP system simulates this mechanism.

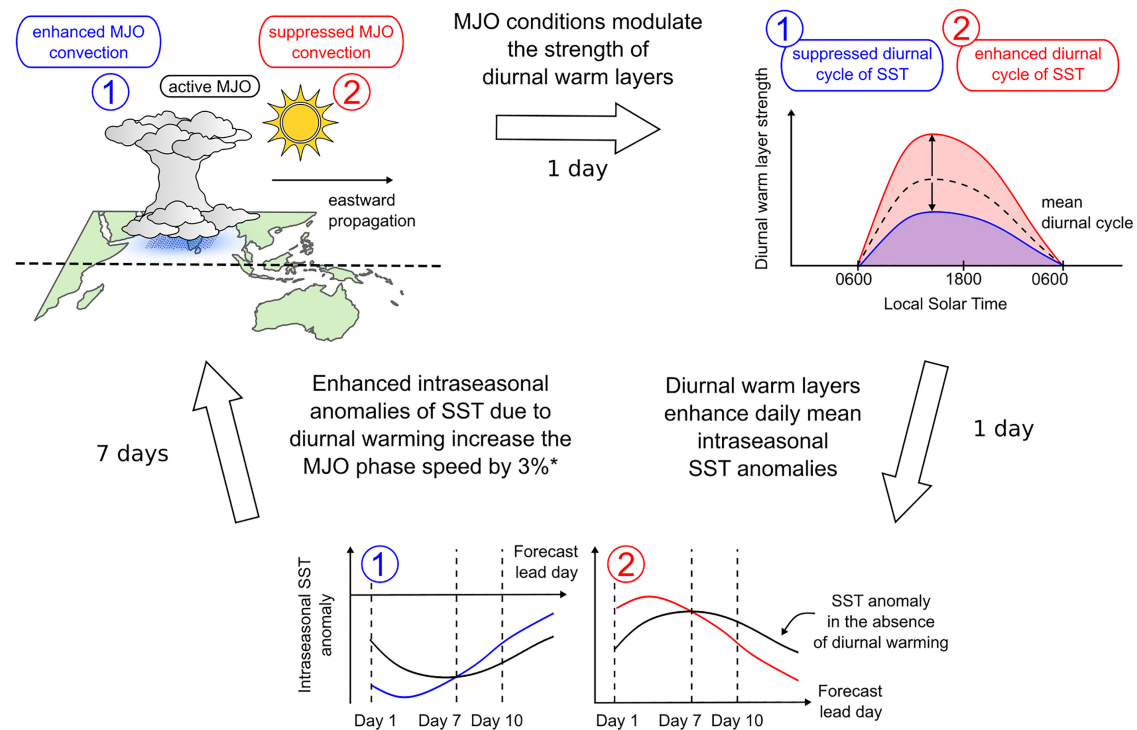
At longer lead times, the coupled model produces a faster MJO due to interactions between the MJO, the dSST, and the SST anomalies (see summary in Figure 12). Changes in the MJO regime lead to changes in the MJO anomalies of dSST. Changes in the MJO anomalies of dSST lead to changes in the amplitude of MJO SST anomalies. Stronger MJO anomalies of dSST at the beginning of the forecast can shift the peak of the MJO anomalies of SST earlier by a few forecast days. The peak

response in the MJO convection to the initial changes in the MJO anomalies of SST is observed on a seven-lead-day timescale in the coupled model. Subsequently, the MJO anomalies of SST respond to these changes in the MJO convection within three days. A stronger warming (or cooling) after the active-to-suppressed MJO transition (or suppressed-to-active MJO transition) is observed for stronger MJO anomalies of dSST. The overall effects of a muted dSST in the coupled model are thus muted MJO anomalies of SST prior to and post the MJO passage, ultimately leading to a slower eastward propagation of the MJO. DeMott *et al.* (2016) showed that stronger fluctuations in SSTs ahead of the MJO lead to more moist static energy there, encouraging MJO convection. Seo *et al.* (2014) showed that higher dSST in a coupled model leads to higher mean SST and higher latent heat flux prior to convection, thus influencing the MJO. This mechanism is similar to that seen here in the coupled model, and we confirm the early hypotheses of Bernie *et al.* (2008) and Woolnough *et al.* (2007) that indeed the presence of the dSST does alter the simulated MJO in a coupled model.

Ultimately, the presence of dSST in this coupled NWP model leads to prediction of an erroneously fast MJO. The atmosphere-only model predicts a more accurate MJO phase speed than the coupled model, according to the verification dataset. The coupled model became the operational forecast model at the Met Office in May 2022, taking over from the atmosphere-only model. The coupled model is more realistic, but introduces more complexity. Convection in the Unified Model (UM: the atmosphere component of the coupled and the atmosphere-only models) is parameterised and may have been tuned to produce a good diurnal cycle of convection with diurnally fixed SSTs. It is possible that the parameterisation scheme oversimulates the diurnal cycle of convection in response to diurnally evolving SSTs in the coupled model, leading to too-fast MJO propagation in this model. Several studies demonstrate the importance of the diurnal cycle of convection and precipitation over the MC (e.g., Baranowski *et al.*, 2019; Birch *et al.*, 2016; Hagos *et al.*, 2016; Peatman *et al.*, 2014; Wei *et al.*, 2020). Generally, the diurnal cycle of precipitation is represented better in convection-permitting models than in the models that parameterise convection (Prein *et al.*, 2015). Senior *et al.* (2023) showed that the regional version of the UM at a convection-permitting horizontal resolution improves extreme rainfall compared with the global lower resolution model that uses parameterised convection. This improvement was associated with the modulation of the diurnal cycle of convection by convectively coupled Kelvin waves, often associated with the MJO (e.g., Neena *et al.*, 2022). If the convection-permitting model improves the diurnal



## Feedback between the MJO and diurnal warm layers



\*in a coupled ocean-atmosphere Numerical Weather Prediction model

**FIGURE 12** Schematic diagram of the two-way feedback between the Madden–Julian Oscillation (MJO) and diurnal warm layers in the upper ocean in the coupled ocean–atmosphere NWP system of the UK Met Office. The MJO conditions in the coupled model modulate the strength of diurnal warm layers at lead day 1 such that enhanced (suppressed) MJO phase leads to suppressed (enhanced) diurnal warm layers. The presence of diurnal warm layers changes the daily mean sea-surface temperatures (SST) in the coupled model and enhances daily mean intraseasonal SST anomalies. Stronger (weaker) diurnal warming at lead day 1 leads to warmer (colder) intraseasonal anomalies of SST than in the absence of diurnal warming. The modulated intraseasonal SST anomalies affect the surface fluxes between the ocean and the atmosphere, and ultimately lead to a peak MJO convection response on a seven-lead-day timescale and a  $\sim 3\%$  increase in the MJO phase speed. Subsequently, the intraseasonal anomalies of SST respond to these MJO convection changes within the next 3 forecast days.

cycle of convection, would the too-fast MJO manifest in this coupled NWP system as well?

Our study also provides implications for climate projections of the MJO. Ahn *et al.* (2020) analysed over 30 Coupled Model Intercomparison Project Phase 5 (CMIP5) and Phase 6 (CMIP6) models to reveal that the improvement in the eastward propagation of the MJO in the CMIP6 models compared with the CMIP5 models is associated with a stronger horizontal moisture gradient in the lower troposphere across the warm-pool region. They showed that the climate configuration of the coupled model examined here (HadGEM3) generates an accurate amplitude of MJO-associated rainfall over the MC. However, similar to our results, the MJO in the HadGEM3 model propagates faster to the east than the observations suggest. The climate model uses the same horizontal resolution in the ocean and the atmosphere as the coupled model here,

therefore this too-fast propagating MJO in the climate setting is likely to be partially caused by the presence of diurnal warm layers in the upper ocean. Unlike the models of the UK Met Office, the majority of the ocean models from CMIP6 do not have a 1-m near-surface resolution (see tab. 1 in Wang *et al.*, 2022). Would the MJO improve or degrade in CMIP models should the near-surface vertical resolution be increased?

In summary, the mechanisms discussed in this article show that the diurnal warming of SST has an important impact on air–sea interactions on MJO timescales in an NWP setting. The two-way feedback between the MJO and diurnal warm layers should be verified further with in situ observations of the diurnal cycle of SST, and the representation of the diurnal cycle of SST should be considered in future model developments in order to achieve better MJO predictions.

## ACKNOWLEDGEMENTS

E. Karłowska was supported by the Natural Environment Research Council and ARIES DTP [grant number NE/S007334/1]. A. J. Matthews was partially funded by the Natural Environment Research Council TerraMaris project [grant NE/R016704/1].

## CONFLICT OF INTEREST STATEMENT

The authors declare no conflict of interest.

## DATA AVAILABILITY STATEMENT

The data that support the findings of this study are available on request from the corresponding author.

## ENDNOTES

<sup>1</sup>Retrieved from <http://www.bom.gov.au/climate/mjo>.

<sup>2</sup>The ATM model uses persisted foundation SSTs from the previous day OSTIA SST in the hindcast mode. Therefore, the ATM model SST at lead day 1 is similar to the foundation SST, albeit lagged by 2 days (not shown).

<sup>3</sup>20–200-day bandpass filtered anomalies.

## ORCID

Eliza Karłowska  <https://orcid.org/0000-0003-2401-0871>

Adrian J. Matthews  <https://orcid.org/0000-0003-0492-1168>

Benjamin G. M. Webber  <https://orcid.org/0000-0002-8812-5929>

## REFERENCES

- Ahn, M., Kim, D., Kang, D., Lee, J., Sperber, K.R., Gleckler, P.J. et al. (2020) MJO propagation across the maritime continent: Are CMIP6 models better than CMIP5 models? *Geophysical Research Letters*, 47, e2020GL087250. Available from: <https://onlinelibrary.wiley.com/doi/10.1029/2020GL087250>
- Anderson, S.P., Weller, R.A. & Lukas, R.B. (1996) Surface buoyancy forcing and the mixed layer of the western pacific warm pool: Observations and 1D model results. *Journal of Climate*, 9, 3056–3085. Available from: <https://journals.ametsoc.org/view/journals/clim/9/12/1520-0442&uscore;1996&uscore;009&uscore;3056&uscore;sbfatm&uscore;2&uscore;0&uscore;co&uscore;2.xml>
- Baranowski, D.B., Waliser, D.E., Jiang, X., Ridout, J.A. & Flatau, M.K. (2019) Contemporary GCM fidelity in representing the diurnal cycle of precipitation over the maritime continent. *Journal of Geophysical Research: Atmospheres*, 124, 747–769. Available from: <https://agupubs.onlinelibrary.wiley.com/doi/10.1029/2018JD029474>
- Bellenger, H. & Duvel, J.-P. (2009) An analysis of tropical ocean diurnal warm layers. *Journal of Climate*, 22, 3629–3646. Available from: <https://journals.ametsoc.org/view/journals/clim/22/13/2008jcli2598.1.xml>
- Bernie, D.J., Guilyardi, E., Madec, G., Slingo, J.M. & Woolnough, S.J. (2007) Impact of resolving the diurnal cycle in an ocean–atmosphere GCM. Part 1: A diurnally forced OGCM. *Climate Dynamics*, 29, 575–590.
- Bernie, D.J., Guilyardi, E., Madec, G., Slingo, J.M., Woolnough, S.J. & Cole, J. (2008) Impact of resolving the diurnal cycle in an ocean–atmosphere GCM. Part 2: A diurnally coupled CGCM. *Climate Dynamics*, 31, 909–925. Available from: <https://link.springer.com/article/10.1007/s00382-008-0429-z>
- Birch, C.E., Webster, S., Peatman, S.C., Parker, D.J., Matthews, A.J., Li, Y. et al. (2016) Scale interactions between the MJO and the western maritime continent. *Journal of Climate*, 29, 2471–2492. Available from: <https://journals.ametsoc.org/view/journals/clim/29/7/jcli-d-15-0557.1.xml>
- Blockley, E.W., Martin, M.J., McLaren, A.J., Ryan, A.G., Waters, J., Lea, D.J. et al. (2014) Recent development of the Met Office operational ocean forecasting system: An overview and assessment of the new Global FOAM forecasts.
- DeMott, C.A., Benedict, J.J., Klingaman, N.P., Woolnough, S.J. & Randall, D.A. (2016) Diagnosing ocean feedbacks to the MJO: SST-modulated surface fluxes and the moist static energy budget. *Journal of Geophysical Research: Atmospheres*, 121, 8350–8373. Available from: <https://agupubs.onlinelibrary.wiley.com/doi/10.1002/2016JD025098>
- Donlon, C.J., Martin, M., Stark, J., Roberts-Jones, J., Fiedler, E. & Wimmer, W. (2012) The operational sea surface temperature and sea ice analysis (OSTIA) system. *Remote Sensing of Environment*, 116, 140–158.
- Drushka, K., Gille, S.T. & Sprintall, J. (2014a) The diurnal salinity cycle in the tropics. *Journal of Geophysical Research: Oceans*, 119, 5874–5890. Available from: <https://agupubs.onlinelibrary.wiley.com/doi/10.1002/2014JC009924>
- Drushka, K., Sprintall, J. & Gille, S.T. (2014b) Subseasonal variations in salinity and barrier-layer thickness in the eastern equatorial Indian Ocean. *Journal of Geophysical Research: Oceans*, 119, 805–823. Available from: <https://agupubs.onlinelibrary.wiley.com/doi/10.1002/2013JC009422>
- Duchon, C.E. (1979) Lanczos filtering in one and two dimensions. *Journal of Applied Meteorology and Climatology*, 18, 1016–1022.
- Fairall, C.W., Bradley, E.F., Godfrey, J.S., Wick, G.A., Edson, J.B. & Young, G.S. (1996) Cool-skin and warm-layer effects on sea surface temperature. *Journal of Geophysical Research: Oceans*, 101, 1295–1308.
- Fiedler, E.K., Mao, C., Good, S.A., Waters, J. & Martin, M.J. (2019) Improvements to feature resolution in the OSTIA sea surface temperature analysis using the NEMOVAR assimilation scheme. *Quarterly Journal of the Royal Meteorological Society*, 145, 3609–3625. Available from: <https://rmets.onlinelibrary.wiley.com/doi/10.1002/qj.3644>
- Ge, X., Wang, W., Kumar, A. & Zhang, Y. (2017) Importance of the vertical resolution in simulating SST diurnal and intraseasonal variability in an oceanic general circulation model. *Journal of Climate*, 30, 3963–3978. Available from: [www.ametsoc.org/PUBSReuseLicenses](http://www.ametsoc.org/PUBSReuseLicenses)
- Good, S., Fiedler, E., Mao, C., Martin, M.J., Maycock, A., Reid, R. et al. (2020) The current configuration of the OSTIA system for operational production of foundation sea surface temperature and ice concentration analyses. *Remote Sensing*, 12, 720. Available from: [www.mdpi.com/journal/remotesensing](http://www.mdpi.com/journal/remotesensing)
- Gottschalck, J., Wheeler, M., Weickmann, K., Vitart, F., Savage, N., Lin, H. et al. (2010) A framework for assessing operational

- Madden-Julian oscillation forecasts: A clivar MJO working group project. *Bulletin of the American Meteorological Society*, 91, 1247–1258. Available from: [www.usclivar.org/organization/mjo&uscore;wg.html](http://www.usclivar.org/organization/mjo&uscore;wg.html)
- Gregory, D. & Allen, S. (1991). The effect of convective downdraughts upon NWP and climate simulations. In *Ninth conference on numerical weather prediction*. Denver, Colorado, pp. 122–123.
- Gregory, D. & Rowntree, P.R. (1990) A mass flux convection scheme with representation of cloud ensemble characteristics and stability-dependent closure. *Monthly Weather Review*, 118, 1483–1506. Available from: <https://journals.ametsoc.org/view/journals/mwre/118/7/1520-0493&uscore;1990&uscore;118&uscore;1483&uscore;amfcs&uscore;2&uscore;0&uscore;co&uscore;2.xml>
- Hagos, S.M., Zhang, C., Feng, Z., Burleyson, C.D., De Mott, C., Kerns, B. et al. (2016) The impact of the diurnal cycle on the propagation of Madden-Julian Oscillation convection across the Maritime Continent. *Journal of Advances in Modeling Earth Systems*, 8, 1552–1564.
- Hendon, H.H. & Glick, J. (1997) Intraseasonal Air–Sea interaction in the tropical Indian and Pacific Oceans. *Journal of Climate*, 10, 647–661. Available from: <https://journals.ametsoc.org/view/journals/clim/10/4/1520-0442&uscore;1997&uscore;010&uscore;0647&uscore;iasit&uscore;2.0.co&uscore;2.xml>
- Hsu, J.Y., Hendon, H., Feng, M. & Zhou, X. (2019) Magnitude and phase of diurnal SST variations in the ACCESS-S1 model during the suppressed phase of the MJOs. *Journal of Geophysical Research: Oceans*, 124, 9553–9571. Available from: <https://agupubs.onlinelibrary.wiley.com/doi/10.1029/2019JC015458>
- Itterly, K., Taylor, P. & Roberts, J.B. (2021) Satellite perspectives of sea surface temperature diurnal warming on atmospheric moistening and radiative heating during MJO. *Journal of Climate*, 34, 1203–1226. Available from: <https://journals.ametsoc.org/view/journals/clim/34/3/JCLI-D-20-0350.1.xml>
- Jiang, X. (2017) Key processes for the eastward propagation of the Madden-Julian Oscillation based on multimodel simulations. *Journal of Geophysical Research: Atmospheres*, 122, 755–770. Available from: <https://agupubs.onlinelibrary.wiley.com/doi/10.1002/2016JD025955>
- Karlowka, E., Matthews, A.J., Webber, B.G.M., Graham, T. & Xavier, P. (2024). The effect of diurnal warming of sea-surface temperatures on the propagation speed of the Madden–Julian oscillation. *Quarterly Journal of the Royal Meteorological Society*, 150, 334–354. Available from: <https://rmets.onlinelibrary.wiley.com/doi/abs/10.1002/qj.4599>
- Kim, H., Janiga, M.A. & Pegion, K. (2019) MJO propagation processes and mean biases in the SubX and S2S reforecasts. *Journal of Geophysical Research: Atmospheres*, 124, 9314–9331. Available from: <https://agupubs.onlinelibrary.wiley.com/doi/full/10.1029/2019JD031139>
- Kim, H.M., Webster, P.J., Toma, V.E. & Kim, D. (2014) Predictability and prediction skill of the MJO in two operational forecasting systems. *Journal of Climate*, 27, 5364–5378. Available from: <http://old.ecmwf>
- Kim, H.-R., Ha, K.-J., Moon, S., Oh, H. & Sharma, S. (2020) Impact of the Indo-Pacific Warm Pool on the Hadley, Walker, and Monsoon Circulations. *Atmosphere*, 11, 1030. Available from: <https://www.mdpi.com/2073-4433/11/10/1030>
- Liebmann, B. & Smith, C.A. (1996) Description of a complete (interpolated) outgoing longwave radiation dataset. *Bulletin of the American Meteorological Society*, 77, 1275–1277. Available from: <http://www.jstor.org/stable/26233278>
- Lim, Y., Son, S.W. & Kim, D. (2018) MJO prediction skill of the subseasonal-to-seasonal prediction models. *Journal of Climate*, 31, 4075–4094. Available from: [www.ametsoc.org/PUBSReuseLicenses](http://www.ametsoc.org/PUBSReuseLicenses)
- Lin, H., Brunet, G. & Derome, J. (2008) Forecast skill of the Madden-Julian oscillation in two Canadian atmospheric models. *Monthly Weather Review*, 136, 4130–4149. Available from: <https://journals.ametsoc.org/view/journals/mwre/136/11/2008mwr2459.1.xml>
- Madden, R.A. & Julian, P.R. (1971) Detection of a 40–50 day oscillation in the zonal wind in the tropical Pacific. *Journal of the atmospheric sciences*, 28, 702–708.
- Madden, R.A. & Julian, P.R. (1972) Description of global-scale circulation cells in the tropics with a 40–50 day period. *Journal of the atmospheric sciences*, 29, 1109–1123.
- Madec, G., Bourdallé-Badie, R., Bouttier, P.-A., Bricaud, C., Bruciaferri, D., Calvert, D. et al. (2017) NEMO ocean engine.
- Matthews, A.J. (2004) Atmospheric response to observed intraseasonal tropical sea surface temperature anomalies. *Geophysical Research Letters*, 31, L14107. Available from: <https://agupubs.onlinelibrary.wiley.com/doi/10.1029/2004GL020474>
- Matthews, A.J., Baranowski, D.B., Heywood, K.J., Flatau, P.J. & Schmidtko, S. (2014) The surface diurnal warm layer in the Indian Ocean during CINDY/DYNAMO. *Journal of Climate*, 27, 9101–9122. Available from: <https://journals.ametsoc.org/view/journals/clim/27/24/jcli-d-14-00222.1.xml>
- Megann, A.P., Storkey, D., Aksenov, Y., Alderson, S., Calvert, D., Graham, T. et al. (2014) Go 5.0: The joint NERC-Met office NEMO global ocean model for use in coupled and forced applications. *Geotechnical Model Development*, 7, 1069–1092.
- Moteki, Q., Katsumata, M., Yoneyama, K., Ando, K. & Hasegawa, T. (2018) Drastic thickening of the barrier layer off the western coast of Sumatra due to the Madden-Julian oscillation passage during the Pre-Years of the Maritime Continent campaign. *Progress in Earth and Planetary Science*, 5, 35. Available from: <https://doi.org/10.1186/s40645-018-0190-9>
- Neena, J.M., Suhas, E. & Jiang, X. (2022) Modulation of the Convectively Coupled Kelvin Waves by the MJO over Different Domains. *Journal of Climate*, 35, 7025–7039. Available from: <https://journals.ametsoc.org/view/journals/clim/35/21/JCLI-D-21-0641.1.xml>
- Peatman, S.C., Matthews, A.J. & Stevens, D.P. (2014) Propagation of the Madden-Julian Oscillation through the Maritime Continent and scale interaction with the diurnal cycle of precipitation. *Quarterly Journal of the Royal Meteorological Society*, 140, 814–825. Available from: <http://doi.wiley.com/10.1002/qj.2161>
- Prein, A.F., Langhans, W., Fosser, G., Ferrone, A., Ban, N., Goergen, K. et al. (2015) A review on regional convection-permitting climate modeling: Demonstrations, prospects, and challenges. *Reviews of geophysics*, 53, 323–361.
- Rae, J.G., Hewitt, H.T., Keen, A.B., Ridley, J.K., West, A.E., Harris, C.M. et al. (2015) Development of the Global Sea Ice 6.0 CICE configuration for the Met Office Global Coupled model. *Geoscientific Model Development*, 8, 2221–2230.



- Rashid, H.A., Hendon, H.H., Wheeler, M.C. & Alves, O. (2011) Prediction of the Madden-Julian oscillation with the POAMA dynamical prediction system. *Climate Dynamics*, 36, 649–661. Available from: <http://www.usclivar.org/mjo.php>
- Rawlins, F., Ballard, S.P., Bovis, K.J., Clayton, A.M., Li, D., Inverarity, G.W. et al. (2007) The met office global four-dimensional variational data assimilation scheme. *Quarterly Journal of the Royal Meteorological Society*, 133, 347–362. Available from: [www.interscience.wiley.com](http://www.interscience.wiley.com)
- Ridley, J.K., Blockley, E.W., Keen, A.B., Rae, J.G., West, A.E. & Schroeder, D. (2018) The sea ice model component of HadGEM3-GC3.1. *Geoscientific Model Development*, 11, 713–723.
- Ruppert, J.H. & Johnson, R.H. (2015) Diurnally modulated cumulus moistening in the preonset stage of the Madden-Julian Oscillation during DYNAMO. *Journal of the Atmospheric Sciences*, 72, 1622–1647. Available from: <https://journals.ametsoc.org/view/journals/atsc/72/4/jas-d-14-0218.1.html>
- Senior, N.V., Matthews, A.J., Webber, B.G.M., Webster, S., Jones, R.W., Permana, D.S. et al. (2023) Extreme precipitation at Padang, Sumatra triggered by convectively coupled Kelvin waves. *Quarterly Journal of the Royal Meteorological Society*, 149, 2281–2300.
- Seo, H., Subramanian, A.C., Miller, A.J. & Cavanaugh, N.R. (2014) Coupled impacts of the diurnal cycle of sea surface temperature on the Madden-Julian Oscillation. *Journal of Climate*, 27, 8422–8443. Available from: <https://journals.ametsoc.org/view/journals/clim/27/22/jcli-d-14-00141.1.html>
- Storkey, D., Blaker, A.T., Mathiot, P., Megann, A., Aksenov, Y., Blockley, E.W. et al. (2018) UK Global Ocean GO6 and GO7: A traceable hierarchy of model resolutions. *Geoscientific Model Development*, 11, 3187–3213.
- Suematsu, T. & Miura, H. (2022) Changes in the eastward movement speed of the Madden-Julian oscillation with fluctuation in the walker circulation. *Journal of Climate*, 35, 211–225. Available from: <https://journals.ametsoc.org/view/journals/clim/35/1/JCLI-D-21-0269.1.html>
- Tseng, W.L., Tsuang, B.J., Keenlyside, N.S., Hsu, H.H. & Tu, C.Y. (2015) Resolving the upper-ocean warm layer improves the simulation of the Madden-Julian oscillation. *Climate Dynamics*, 44, 1487–1503. Available from: <https://link.springer.com/article/10.1007/s00382-014-2315-1>
- Vellinga, M., Copsey, D., Graham, T., Milton, S. & Johns, T. (2020) Evaluating benefits of two-way ocean-atmosphere coupling for global NWP forecasts. *Weather and Forecasting*, 35, 2127–2144. Available from: <https://journals.ametsoc.org/view/journals/wefo/35/5/wafD200035.html>
- Vitart, F. (2017) Madden-Julian Oscillation prediction and teleconnections in the S2S database. *Quarterly Journal of the Royal Meteorological Society*, 143, 2210–2220. Available from: <https://onlinelibrary.wiley.com/doi/10.1002/qj.3079>
- Walters, D., Baran, A.J., Boutle, I., Brooks, M., Earnshaw, P., Edwards, J. et al. (2019) The Met Office Unified Model Global Atmosphere 7.0/7.1 and JULES Global Land 7.0 configurations. *Geoscientific Model Development*, 12, 1909–1963.
- Walters, D., Boutle, I., Brooks, M., Melvin, T., Stratton, R., Vosper, S. et al. (2017) The Met Office Unified Model Global Atmosphere 6.0/6.1 and JULES Global Land 6.0/6.1 configurations. *Geoscientific Model Development*, 10, 1487–1520.
- Wang, Y., Heywood, K.J., Stevens, D.P. & Damerell, G.M. (2022) Seasonal extrema of sea surface temperature in CMIP6 models. *Ocean Science*, 18, 839–855.
- Waters, J., Lea, D.J., Martin, M.J., Mirouze, I., Weaver, A. & While, J. (2015) Implementing a variational data assimilation system in an operational 1/4 degree global ocean model. *Quarterly Journal of the Royal Meteorological Society*, 141, 333–349. Available from: <https://rmets.onlinelibrary.wiley.com/doi/full/10.1002/qj.2388>
- Wei, Y., Pu, Z. & Zhang, C. (2020) Diurnal Cycle of Precipitation Over the Maritime Continent Under Modulation of MJO: Perspectives From Cloud-Permitting Scale Simulations. *Journal of Geophysical Research: Atmospheres*, 125, e2020JD032529. Available from: <https://agupubs.onlinelibrary.wiley.com/doi/abs/10.1029/2020JD032529>
- Wheeler, M.C. & Hendon, H.H. (2004) An All-Season Real-Time Multivariate MJO Index: Development of an Index for Monitoring and Prediction. Tech. rep.
- Woolnough, S.J., Slingo, J.M. & Hoskins, B.J. (2000) The Relationship between Convection and Sea Surface Temperature on Intraseasonal Timescales. *Journal of Climate*, 13, 2086–2104. Available from: <https://journals.ametsoc.org/view/journals/clim/13/12/1520-0442&uscore;2000&uscore;013&uscore;2086&uscore;trbcas&uscore;2.0.co&uscore;2.xml>
- Woolnough, S.J., Slingo, J.M. & Hoskins, B.J. (2001) The organization of tropical convection by intraseasonal sea surface temperature anomalies. *Quarterly Journal of the Royal Meteorological Society*, 127, 887–907. Available from: <https://rmets.onlinelibrary.wiley.com/doi/abs/10.1002/qj.49712757310>
- Woolnough, S.J., Vitart, F. & Balmaseda, M.A. (2007) The role of the ocean in the Madden-Julian Oscillation: Implications for MJO prediction. *Quarterly Journal of the Royal Meteorological Society*, 133, 117–128. Available from: <http://doi.wiley.com/10.1002/qj.4>
- Xiang, B., Zhao, M., Jiang, X., Lin, S.J., Li, T., Fu, X. et al. (2015) The 3–4-week MJO prediction skill in a GFDL coupled model. *Journal of Climate*, 28, 5351–5364. Available from: <https://journals.ametsoc.org/view/journals/clim/28/13/jcli-d-15-0102.1.html>
- Yan, X.H., Ho, C.R., Zheng, Q. & Klemas, V. (1992) Temperature and size variabilities of the Western Pacific Warm Pool. *Science*, 258, 1643–1645. Available from: <https://www.science.org>
- Yan, Y., Zhang, L., Yu, Y., Chen, C., Xi, J. & Chai, F. (2021) Rectification of the Intraseasonal SST Variability by the Diurnal Cycle of SST Revealed by the Global Tropical Moored Buoy Array. *Geophysical Research Letters*, 48, e2020GL090913. Available from: <https://agupubs.onlinelibrary.wiley.com/doi/10.1029/2020GL090913>

**How to cite this article:** Karlowska, E., Matthews, A.J., Webber, B.G.M., Graham, T. & Xavier, P. (2024) Two-way feedback between the Madden-Julian Oscillation and diurnal warm layers in a coupled ocean-atmosphere model. *Quarterly Journal of the Royal Meteorological Society*, 150(764), 4113–4132. Available from: <https://doi.org/10.1002/qj.4807>